Focus Section: 2018 Anchorage Earthquake

Seismic Response of Cook Inlet Sedimentary Basin, Southern Alaska

Kyle Smith*[1] and Carl Tape[1]

Abstract

Cook Inlet fore-arc basin in south-central Alaska is a large, deep (7.6 km) sedimentary basin with the Anchorage metropolitan region on its margins. From 2015 to 2017, a set of 28 broadband seismic stations was deployed in the region as part of the Southern Alaska Lithosphere and Mantle Observation Network (SALMON) project. The SALMON stations, which also cover the remote western portion of Cook Inlet basin and the back-arc region, form the basis for our observational study of the seismic response of Cook Inlet basin. We quantify the influence of Cook Inlet basin on the seismic wavefield using three data sets: (1) ambient-noise amplitudes of 18 basin stations relative to a nonbasin reference station, (2) earthquake ground-motion metrics for 34 crustal and intraslab earthquakes, and (3) spectral ratios (SRs) between basin stations and nonbasin stations for the same earthquakes. For all analyses, we examine how quantities vary with the frequency content of the seismic signal and with the basin depth at each station. Seismic waves from earthquakes and from ambient noise are amplified within Cook Inlet basin. At low frequencies (0.1–0.5 Hz), ambient-noise ratios and earthquake SRs are in a general agreement with power amplification of 6–14 dB, corresponding to amplitude amplification factors of 2.0–5.0. At high frequencies (0.5–4.0 Hz), the basin amplifies the earthquake wavefield by similar factors. Our results indicate stronger amplification for the deeper basin stations such as near Nikiski on the Kenai Peninsula and weaker amplification near the margins of the basin. Future work devoted to 3D wavefield simulations and treatment of source and propagation effects should improve the characterization of the frequency-dependent response of Cook Inlet basin to recorded and scenario earthquakes in the region.

Cite this article as Smith, K., and C. Tape (2019). Seismic Response of Cook Inlet Sedimentary Basin, Southern Alaska, *Seismol. Res. Lett.* **91**, 33–55, doi: 10.1785/0220190205.

Supplemental Material

Introduction

Cook Inlet basin is a fore-arc sedimentary basin that is part of the Alaska subduction zone and borders the metropolitan region that includes Anchorage, Eagle River, Chugiak, Wasilla, and Palmer. The basin is 250 km long and 100 km wide (Fig. 1a) and is one of the largest active fore-arc basins in the world (Clift and Vannucchi, 2004). Cook Inlet has been a site of sedimentary deposition for most of the past 160 Ma, with a maximal Mesozoic thickness of 12 km and a maximal Tertiary thickness of 7.6 km (Fisher and Magoon, 1978; Shellenbaum *et al.*, 2010). The lowermost Tertiary units were used by Shellenbaum *et al.* (2010) to define a detailed basement surface having a maximal depth of 7.6 km near Nikiski, on the western Kenai Peninsula (Fig. 1a; ZE.NSKI in Fig. 2), and overlying Mesozoic strata (Gregersen and Shellenbaum, 2016).

The Cook Inlet region is highly seismically active, with earthquakes $M_w > 7$ in both the subducting slab and within the crust. Notable intraslab earthquakes include the 1954-10-03 M_w 6.4 earthquake under the Kenai Peninsula (Doser and Brown, 2001; Silwal *et al.*, 2018), the 2016-01-24 M_w 7.1 earthquake southwest of the basin (Grapenthin *et al.*, 2018), and the 2018-11-30 M_w 7.1 earthquake beneath Anchorage (Liu *et al.*, 2019; West *et al.*, 2019). Notable crustal earthquakes include the 1933-04-27 M_w 6.8 earthquake just below Cook Inlet basin (perhaps within the Mesozoic strata) and the 1943-11-03 M_w 7.3 earthquake in the Susitna region north of Cook Inlet basin (Silwal *et al.*, 2018). The subduction megathrust is partially locked and last ruptured in the 1964-03-28 M_w 9.2 Prince William Sound earthquake (Zweck *et al.*, 2002). Few moderate ($M_w > 4$) earthquakes seem to occur on the interface (Li *et al.*, 2013) during the interseismic period between $M_w > 8$ ruptures and their aftershocks.

Our study focuses on a time period from May 2015 to July 2017 spanning the deployment of 28 broadband seismometers in the Cook Inlet region (Tape *et al.*, 2017). A primary scientific objective of the 2 yr deployment (Southern Alaska Lithosphere

1. Geophysical Institute, University of Alaska Fairbanks, Fairbanks, Alaska, U.S.A.
*Corresponding author: kksmith7@alaska.edu

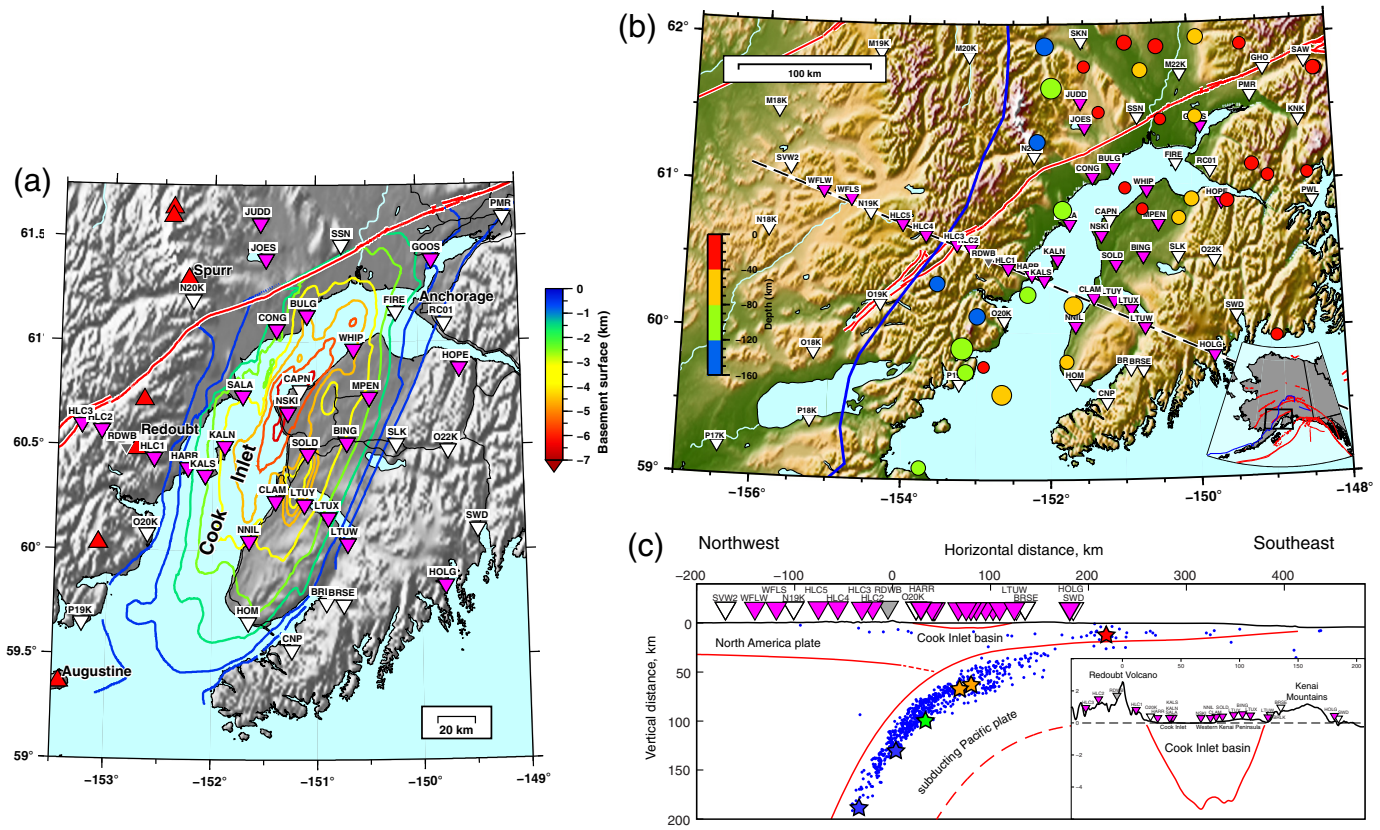

Figure 1. The Cook Inlet region, with seismic stations (2015–2017) and earthquakes used in this study. Southern Alaska Lithosphere and Mantle Observation Network stations are plotted as magenta inverted triangles; other broadband stations are white. Active faults of Koehler *et al.* (2012) are plotted in red. (a) Cook Inlet basin: contours are for the base-Tertiary basement map of Shellenbaum *et al.* (2010). Red upright triangles are active volcanoes. (b) Earthquakes and stations within the full study region. The 34 earthquakes analyzed in this study (Table 1) are colored by depth and sized by magnitude. The Redoubt line of stations extends from AT.SVW2 in the west, through Redoubt Volcano, and to ZE.HOLG on the eastern Kenai Peninsula. Inset map shows Alaska, with a box denoting the study region of (b). (c) Cross section of seismicity within 50 km of the Redoubt line and occurring between 2015-05-01 and 2017-08-01, $M_L \geq 2.0$. There are six events (of 34 in our analysis) that are plotted as stars and within this corridor of seismicity. Stations within 50 km of the Redoubt line are also shown. Cook Inlet basin basement map from Shellenbaum *et al.* (2010), continental Moho from Wang and Tape (2014), and subduction interface from Hayes *et al.* (2018). The color version of this figure is available only in the electronic edition.

and Mantle Observation Network [SALMON]) was to understand the influence of Cook Inlet basin on the seismic wavefield. The full set of stations considered for analysis is shown in the region of Figure 1b and tabulated in Figure 2.

The SALMON seismic stations provide an opportunity to investigate how Cook Inlet basin influences the seismic wavefield, both from earthquakes and from continuous ambient noise. A preliminary study based on the first year of SALMON data showed amplification of seismic noise in basin stations, as well as a correlation between basin depth and ground-motion amplitudes filtered at 1.8–4 s, for one intraslab earthquake (Tape *et al.*, 2017). In this study, we examine a total of 34 earthquakes recorded at 48 stations, including SALMON stations, EarthScope (TA) stations, and the permanent networks (AK, AV). Using earthquake recordings and ambient noise, we document basin amplification of 6–14 dB, corresponding to amplitude amplification factors of 2.0–5.0, for low frequencies (0.1–0.5 Hz). At high frequencies (0.5–4.0 Hz), the basin amplifies the earthquake wavefield by similar factors. Further work is needed to account for complexities of 3D structure (elastic and anelastic) and source mechanisms.

Previous Studies of Basin Amplification

Sedimentary basins were acknowledged as a major factor in enhancing ground motions during the M_w 8.0 Mexico City earthquake (Anderson *et al.*, 1986; Bard *et al.*, 1988; Lomnitz, 1988). Some of these studies quoted the "bowl of jelly" metaphor commonly used to describe how sedimentary basins trap seismic waves and resonate (see also Carder, 1963, p. 3). The observation that unconsolidated sediments amplify earthquake ground motions is well established. As pointed out by Borcherdt (1970), the 1908 report on the 1906 M_w 7.9 San Francisco earthquake concluded: "This investigation has clearly demonstrated that the amount of damage produced by the earthquake of April 18 in different parts of the city and county of San Francisco depended chiefly upon the geological character of the ground. Where

	Station	Longitude (°)	Latitude (°)	inoise	Basin depth (km)	ibasin	Distance to basin (km)	Start date	End date
1	AK.CAPN	−151.15	60.77	1	7.3	3	0	2015/01/01	2018/01/01
2	ZE.NSKI	−151.28	60.66	1	7.0	3	0	2015/01/01	2018/01/01
3	ZE.LTUY	−151.12	60.22	1	5.2	3	0	2015/01/01	2018/01/01
4	ZE.SOLD	−151.08	60.46	1	5.2	3	0	2015/01/01	2018/01/01
5	ZE.WHIP	−150.63	60.97	1	5.2	3	0	2015/01/01	2018/01/01
6	ZE.BULG	−151.09	61.13	1	4.9	3	0	2016/01/01	2018/01/01
7	ZE.CLAM	−151.39	60.24	1	4.9	3	0	2015/01/01	2018/01/01
8	ZE.KALN	−151.89	60.50	1	4.3	3	0	2015/01/01	2018/01/01
9	ZE.BING	−150.70	60.52	1	3.7	3	0	2015/01/01	2018/01/01
10	ZE.NNIL	−151.65	60.05	1	3.7	3	0	2015/01/01	2018/01/01
11	ZE.SALA	−151.71	60.74	1	3.7	3	0	2015/01/01	2018/01/01
12	ZE.MPEN	−150.48	60.74	1	3.4	3	0	2016/05/21	2017/05/21
13	ZE.KALS	−152.07	60.36	1	3.0	3	0	2015/06/01	2016/06/01
14	ZE.CONG	−151.39	61.06	1	2.7	3	0	2015/01/01	2018/01/01
15	AK.HOM	−151.65	59.66	1	2.7	3	0	2015/01/01	2018/01/01
16	AK.FIRE	−150.22	61.14	1	2.4	3	0	2015/01/01	2018/01/01
17	ZE.LTUX	−150.88	60.16	1	2.4	3	0	2015/01/01	2018/01/01
18	ZE.GOOS	−149.85	61.39	1	0.9	3	0	2015/01/01	2018/01/01
19	TA.O20K	−152.62	60.08	1	0	2	5	2016/01/01	2018/01/01
20	TA.P19K	−153.23	59.65	1	0	2	11	2017/01/01	2018/01/01
21	AT.PMR	−149.13	61.59	1	0	1	2	2015/01/01	2018/01/01
22	AK.RC01	−149.74	61.09	1	0	1	3	2015/01/01	2018/01/01
23	ZE.LTUW	−150.70	60.03	1	0	1	4	2016/01/01	2018/01/01
24	AK.SLK	−150.22	60.51	1	0	1	6	2015/01/01	2018/01/01
25	AK.BRLK	−150.91	59.75	1	0	1	7	2015/01/01	2018/01/01
26	AK.GHO	−148.93	61.77	1	0	1	8	2015/01/01	2018/01/01
27	AK.SSN	−150.75	61.46	1	0	1	9	2016/07/01	2017/07/01
28	AK.CNP	−151.24	59.53	1	0	1	10	2015/01/01	2018/01/01
29	AK.BRSE	−150.74	59.74	1	0	1	15	2015/01/01	2018/01/01
30	ZE.HOPE	−149.60	60.87	1	0	1	19	2015/01/01	2018/01/01
31	AK.SAW	−148.33	61.81	1	0	0	21	2015/01/01	2018/01/01
32	AV.RDWB	−152.84	60.49	1	0	0	24	2015/08/01	2016/08/01
33	AK.KNK	−148.46	61.41	1	0	0	37	2015/01/01	2018/01/01
34	ZE.HLC2	−153.08	60.58	1	0	0	39	2016/01/01	2018/01/01
35	ZE.HLC3	−153.28	60.60	1	0	0	50	2015/01/01	2018/01/01
36	AK.SWD	−149.45	60.10	1	0	0	62	2017/01/01	2018/01/01
37	ZE.HLC4	−153.71	60.67	1	0	0	74	2016/01/01	2018/01/01
38	AK.SKN	−151.53	61.98	1	0	0	76	2016/06/01	2017/06/01
39	AK.PWL	−148.33	60.86	1	0	0	83	2017/01/01	2018/01/01
40	ZE.HLC5	−154.03	60.74	1	0	0	93	2015/01/01	2018/01/01
41	TA.M20K	−153.13	61.88	1	0	0	102	2017/01/01	2018/01/01
42	TA.N19K	−154.48	60.81	1	0	0	119	2016/01/01	2018/01/01
43	TA.P18K	−155.23	59.39	1	0	0	121	2016/01/01	2018/01/01
44	TA.O18K	−155.21	59.85	1	0	0	123	2016/01/01	2018/01/01
45	ZE.WFLS	−154.76	60.91	1	0	0	136	2015/01/01	2018/01/01
46	TA.M19K	−154.39	61.90	1	0	0	149	2016/01/01	2018/01/01
47	ZE.WFLW	−155.14	60.96	1	0	0	158	2015/01/01	2018/01/01
48	AT.SVW2	−155.62	61.11	1	0	0	185	2015/01/01	2018/01/01
49	ZE.HARR	−152.24	60.40	0	1.5	3	0	2015/01/01	2018/01/01
50	ZE.HLC1	−152.57	60.44	0	0	1	9	2015/01/01	2018/01/01
51	TA.N20K	−152.21	61.20	0	0	1	13	2017/01/01	2018/01/01
52	ZE.JOES	−151.49	61.40	0	0	1	18	2015/01/01	2018/01/01
53	TA.M22K	−150.12	61.75	0	0	1	20	2016/01/01	2018/01/01
54	TA.O22K	−149.72	60.48	0	0	0	31	2015/01/01	2018/01/01
55	ZE.JUDD	−151.55	61.57	0	0	0	37	2015/01/01	2018/01/01
56	ZE.HOLG	−149.77	59.84	0	0	0	59	2015/01/01	2018/01/01
57	TA.O19K	−154.32	60.20	0	0	0	85	2016/01/01	2018/01/01
58	TA.N18K	−155.89	60.68	0	0	0	187	2015/01/01	2018/01/01
59	TA.P17K	−156.44	59.20	0	0	0	190	2017/01/01	2018/01/01
60	TA.M18K	−155.82	61.49	0	0	0	200	2015/01/01	2018/01/01

Figure 2. Broadband seismic stations in the Cook Inlet region (Fig. 1), sorted in decreasing order of basin depth. The first 48 stations (with inoise = 1) are selected for analyses in this study; these are colored as 18 basin stations, 12 marginal basin stations, and 18 nonbasin stations. The start and end dates denote the integer-year time period used in the noise analysis for 48 stations. The color version of this figure is available only in the electronic edition.

the surface was of solid rock, the shock produced little damage; whereas upon made land great violence was manifested" (Lawson 1908, p. 241).

Improvements in theoretical models, numerical models, and instrumentation over the past century have led to a better understanding of how sedimentary basins affect seismic waves (Gutenberg, 1957; Borcherdt, 1970; Bard and Bouchon, 1980, 1985; Rial *et al.*, 1992; Field and Jacob, 1993; Wald and Graves, 1998; Olsen, 2000). The margins of basins can also have a strong influence on the seismic wavefield (Frankel, 1993; Hisada and Yamamoto, 1996; Kawase, 1996; Graves *et al.*, 1998; Joyner, 2000; Frankel *et al.*, 2009; Wirth *et al.*, 2019). Previous work explored the amplification of basin structures from two end-member waves: shear waves entering from below basins and surface waves (Love and Rayleigh) entering from the side of basins (Bard and Bouchon, 1980). Efforts to model basin effects assumed 1D, 2D, and 3D structural representations of basins (Bard *et al.*, 1988; Sánchez-Sesma and Luzón, 1995; Bowden and Tsai, 2017; Feng and Ritzwoller, 2017; Tsai *et al.*, 2017). Examples of data-based studies of specific basins include those by Pratt *et al.* (2003), Bindi *et al.* (2009), Yoshimoto and Takemura (2014), and Moschetti *et al.* (2017).

Numerical modeling and empirical observations have been used to better understand the relationship between basin depth and amplification of seismic waves and to incorporate these effects into ground-motion prediction equations (Choi *et al.*, 2005; Fletcher and Wen, 2005; Day *et al.*, 2008; Cruz-Atienza

et al., 2016). One example of this approach for the Cook Inlet region is Moschetti *et al.* (2020), which examines a suite of regional earthquakes recorded during the SALMON deployment and at other time periods.

Station Selection

We analyze all broadband seismic stations within the region shown in Figure 1b that operated between 2015-01-01 and 2018-01-01. Stations from the AV network are intermediate band and are excluded, with the exception of RDWB on Redoubt Volcano. Our analysis of ambient seismic noise is based on an annual stack of daily spectra. Because ambient seismic noise amplitudes can vary strongly with time, we need to stack over an integer number of years to minimize seasonal bias within the stack. Therefore we exclude any station that does not have an integer number of years (1, 2, or 3) within the time interval of interest. This criterion excludes three SALMON stations (HARR, HLC1, and HOLG) that experienced outages due to bears (Tape *et al.*, 2019) and two TA stations (N18K and N20K) having outages because of power or telemetry issues. Station TA.M18K was not installed until May 2017. Six additional stations are excluded for reasons discussed later.

The 60 stations considered in our analysis (Fig. 1b) are tabulated in Figure 2 and categorized based on their locations relative to the margin of Cook Inlet basin. A basin station is inside the outermost basin contour of (Shellenbaum *et al.*, 2010). A marginal station is outside the outermost basin contour of but within 20 km of the contour. A nonbasin station is at least 20 km outside the outermost basin contour. Our analysis includes 48 stations categorized as 18 basin stations, 12 marginal stations, and 18 nonbasin stations (Fig. 2). Among the 18 basin stations, 15 are from the SALMON experiment, and three are part of the permanent AK network (CAPN, HOM, and FIRE).

We are interested in the amplitudes of ambient noise within Cook Inlet basin, relative to ambient noise outside the basin. There are several nonbasin stations to consider for establishing a nonbasin reference spectrum. We choose AK.SSN, which is a Streckeisen STS-5 sensor installed in bedrock at a depth of 2.71 m in a cased borehole on Susitna Mountain outside the northern margin of Cook Inlet basin (Fig. 1a). The reference noise spectra for SSN are based on a single year of data (2016-07-01 to 2017-07-01) and are used for comparison with spectra from all other stations (e.g., Figs. S1 and S2, available in the supplemental material to this article).

Ambient-noise amplitudes are influenced by local structure, and therefore we might not expect the noise spectrum in the back-arc bedrock region such as at WFLW, to be the same as the noise in the fore-arc bedrock region such as on the southern Kenai Peninsula. Figures S3–S5 show that the noise spectra for stations on the southern Kenai Peninsula (Fig. 1a: AK.CNP, AK.BRLK, AK.BRSE, and AK.SWD; also ZE.HOLG though its data are limited) are similar to each other—suggestive of a regional noise reference—yet different from SSN. We attribute the differences in regional noise reference levels in the back-arc and fore-arc to crustal-scale structural differences between these two nonbasin settings. It is also possible that some differences between back-arc and fore-arc spectra, especially for frequencies >1 Hz, could be related to their different distances from regional ocean-generated noise sources.

After examining the noise spectra (Figs. S3–S8), we created a subclassification for marginal stations for stations exhibiting basin-like spectra. Stations TA.O20K and TA.P19K are outside the Cook Inlet basin and are installed in bedrock, yet their spectra are consistent with those of basin stations overlying 1000s of meters of basin strata. However, the local site conditions at O20K and P19K are bedrock: both sensors are installed at 2.56 m depth in boreholes within "competent bedrock" according to the drill logs. We revisit this topic in the Discussion section.

Some marginal and nonbasin stations are excluded because of anomalous noise levels at high frequencies (Figs. S7 and S8). This includes three marginal stations north of Cook Inlet basin (ZE.JOES, ZE.JUDD, and TA.M22K), one station on the Kenai Peninsula (TA.O22K), and two in the back-arc region southwest of Cook Inlet (TA.P17K and TA.O19K). By excluding these stations, we are left with a set of stations that provide the most representative amplitudes of the regional ambient-noise wavefield. Characteristics from the settings at these excluded stations are helpful in understanding the lowest anomalous noise levels. Next, we describe characteristics at two excluded stations TA.O22K and ZE.JOES.

The sensor at TA.O22K is a Nanometrics Trillium 120PH sensor installed at a depth of 2.31 m in a "Competent layer of slate," as described in the drill log. The enhanced noise above 0.5 Hz (relative to SSN or SLK, which is closer) is likely due to a combination of structural, environmental, and anthropogenic influences. The structural influence could arise from the sedimentary deposits that the station is within. Environmental influences could arise from Kenai Lake (with or without ice), whose shoreline is 360 m to the southwest; the lake is the source of Kenai River. Anthropogenic noise could arise from the Sterling Highway, which is 600 m to the northwest, from boats on Kenai Lake, or from activity on closer, smaller roads.

Station ZE.JOES is excluded because it may be influenced by the structure of Beluga basin (Stanley *et al.*, 2013; Saltus *et al.*, 2016; Silwal *et al.*, 2018), which is situated north of the Castle Mountain fault. JOES is near a remote summer camp on the edge of Beluga Lake, 18 km from the edge of Cook Inlet basin. Its spectra exhibit unusually large discrepancy between H and Z noise spectra for 0.2–1.0 Hz.

Earthquake Selection

Earthquakes were selected between 2015-05-01 and 2017-08-01, aligned with the SALMON experiment (Fig. 1b), to best examine the spatial variations of Cook Inlet basin effects. Because basin effects have been well documented for low frequencies (0.1–1.0 Hz), our focus was to examine the largest earthquakes

recorded within the time period of SALMON. Smaller earthquakes ($M_w < 3$) do not generate sufficient signals at low frequencies. We exclude the largest earthquake, M_w 7.1 on 2016-01-24 (Grapenthin *et al.*, 2018), because it clipped most of the stations in Cook Inlet basin.

Our selection of earthquakes started with all events in the region of Figure 1b between 2015-05-01 and 2017-08-01 and having magnitudes between 3 and 7. With a desire of uniform spatial coverage without highly redundant events, we declustered the 372 events based on a volumetric grid of 8×8 cells, multiplied into depth sheets with boundaries at 30, 60, and 200 km. Within the shallowest layer (0–30 km), we accept two earthquakes per cell having $M_L \geq 3.5$. Within the lower two layers, we accept one earthquake per cell having $M_L \geq 4.0$. These criteria led to a set of 30 earthquakes. To examine excitation of the shallow basin structure, we included all earthquakes with M_L 3.0–3.5 with depths ≤30 km and with epicenters inside the basin boundary of Shellenbaum *et al.* (2010). These criteria resulted in four earthquakes, bringing our total to 34.

The 34 in our analysis are listed in Table 1 and plotted in Figure 1b. The cross section of stations and seismicity in Figure 1c highlights our source–station geometry and our spatial declustering of events: within the 100-km-wide corridor of seismicity, there are six events in our analysis. The majority of the events are smaller crustal earthquakes within the northeast portion of our study region (Fig. 1a).

Ambient Noise

Our analysis of ambient noise in the Cook Inlet region is based on daily power spectral density plots computed and made available by Incorporated Research Institutions for Seismology (IRIS) Modular Utility for STAatistical kNowledge Gathering (MUSTANG; Casey *et al.*, 2018). These acceleration power spectra are log scaled into units of decibels. A table showing a comparison among decibel values, power ratios, and amplification ratios is shown in Table S1.

Methods

Ambient seismic noise amplitudes can be strongly time dependent because of environmental or anthropogenic variations. Therefore, to obtain a representative noise spectrum, one must use a time window that is an integer number of years. The time intervals used to calculate the annual station stacks are listed in Figure 2 for the 48 stations in our analysis.

Our goal is to quantify the frequency-dependent amplification of ambient noise at seismic stations. Our procedure is as follows:

1. For each of the 48 stations, calculate the station's annual spectra for the vertical and horizontal components. An example is shown in Figure 3a.
2. For each station, calculate a differential spectrum by subtracting the annual spectrum of SSN from the station's annual spectrum. An example is shown in Figure 3c.
3. For each differential spectrum, quantify the amplification within two frequency intervals: 0.1–0.5 Hz and 0.5–4.0 Hz. These intervals are chosen based on the characteristics of the differential spectra for 18 basin stations (Fig. S2). Within the first interval, the differential spectra tend to be flat (Fig. 3c,d,g,h), and therefore we measure a median value of the entries between 0.1 and 0.5 Hz. The uncertainty is estimated by the median absolute deviation of values. Within the second interval, which spans high frequencies (hf), the differential spectra are often peaked (Fig. 3c,d,g,h), and therefore we calculate the maximum value, which occurs at $0.5 < f_{hf} < 4.0$. The uncertainty is estimated by calculating the median absolute deviation of $\{A_k(f_{hf}), k = 1, \ldots, 365n\}$, in which A_k is the kth day spectrum used in creating the annual spectrum and n is the number of years used to make the annual spectrum.

Results

Our noise results are summarized in Figures 4 and 5. Figure 4 shows separation between basin spectra (red) and marginal basin spectra (blue) from the nonbasin reference spectrum SSN (black). We will focus our discussion on the vertical-component differential spectra shown in Figure 4d. Over the frequency range 0.1–0.5 Hz, the spectra of 18 basin stations are amplified by 9–15 dB relative to reference station SSN. (Table S1 provides a comparison between power in decibels and amplification factors.) Over the frequency range 0.5–4.0 Hz, the spectra of 18 basin stations are amplified by 15–50 dB relative to reference station SSN. Even at the lowest frequencies (<0.1 Hz), where ground tilting caused by atmospheric effects occurs (Sorrells *et al.*, 1971), there is clear enhancement of noise at basin stations.

Distilling each differential spectrum to two numbers—one for 0.1–0.5 Hz and one for 0.5–4.0 Hz—we can examine the amplification in terms of basin depth at each station (Fig. 5). The patterns visible in Figure 4 are also clear in Figure 5: ambient noise is amplified at basin stations. We color regions in Figure 5 for the sake of discussion: red for basin stations, blue for marginal stations, and green for nonbasin stations.

At low frequencies for both H and Z components, the overall pattern is that for stations with basin depths >2 km, noise levels on the vertical component are 9–15 dB higher than nonbasin station SSN (Fig. 5b). The effect is stronger on the horizontal component (Fig. 5a). There is a weak correlation between basin depth and noise amplitude: GOOS, with 1 km basin depth, has the lowest amplification, while NSKI and CAPN, with 7 km depth have the highest amplification. Also, the two basin-like marginal stations O20K and P19K exhibit similar amplification as GOOS.

The pattern at high frequencies is similar, though the basin amplification values are stronger (15–50 dB), and the variations among sets of stations are also larger. For example, even for nonbasin stations (shaded green in Fig. 5c,d), the noise levels on the vertical component are between −5 and 15 dB of SSN (Fig. 5d), but for low frequencies, the noise

TABLE 1
34 Earthquakes Analyzed in This Study

Origin Time (yyyy/mm/dd hh:mm:ss.sss)	Longitude (°)	Latitude (°)	Depth (km)	Magnitude (M_L)
2015/05/18 15:49:10.522	−150.4504	61.9398	22	4.3
2015/06/24 22:32:21.166	−151.9621	61.6644	114	5.8
2015/07/25 19:57:43.227	−152.0518	61.9493	126	5.2
2015/07/27 02:21:54.395	−150.9390	60.9827	16	3.4
2015/07/29 02:35:59.449	−153.1962	59.8935	119	6.4
2015/11/06 14:26:50.635	−149.8762	61.9965	46	4.4
2016/01/04 02:38:05.283	−148.9329	61.0382	21	3.6
2016/01/24 14:29:28.374	−153.1457	59.7312	107	4.7
2016/02/03 20:31:25.777	−153.5461	60.3334	189	4.5
2016/02/10 14:36:17.399	−152.9050	59.7693	19	3.4
2016/02/15 10:41:46.974	−150.0123	60.8957	48	4.2
2016/02/28 13:48:51.632	−150.6873	61.7805	62	4.3
2016/03/12 21:57:55.683	−152.3041	60.2609	100	4.7
2016/04/08 03:24:18.180	−149.9238	61.4564	40	4.0
2016/04/20 14:55:42.428	−148.1806	61.7490	15	4.0
2016/05/01 20:38:46.663	−152.9931	60.1136	129	4.7
2016/05/30 19:01:29.827	−153.7581	59.0778	103	4.1
2016/08/30 12:27:59.886	−149.1495	61.1186	38	4.0
2016/09/01 12:27:42.774	−152.1646	61.2991	132	4.5
2016/10/02 22:39:41.110	−149.5161	60.8787	24	4.0
2016/10/14 12:59:05.731	−151.7773	59.8029	63	4.0
2016/10/19 00:16:30.695	−148.9192	59.9489	11	3.5
2016/11/06 19:40:49.667	−148.2035	61.7493	12	4.1
2016/11/21 22:27:27.757	−150.1984	60.7706	50	4.0
2016/12/03 08:04:47.085	−150.4189	61.4436	14	3.3
2016/12/04 13:15:44.183	−150.9023	61.9700	9	4.2
2016/12/24 05:24:41.092	−148.3761	61.0454	13	3.5
2017/03/02 02:11:30.682	−152.6546	59.5785	78	5.6
2017/03/17 07:47:31.160	−149.2418	61.9406	3	3.6
2017/04/30 21:32:17.954	−150.7014	60.8369	26	3.3
2017/05/07 04:25:19.095	−151.6783	60.1828	67	5.3
2017/05/07 19:58:25.043	−151.2931	61.4974	17	3.5
2017/05/24 09:59:01.220	−151.4935	61.8085	10	3.5
2017/05/30 02:18:45.889	−151.8152	60.8341	81	5.2

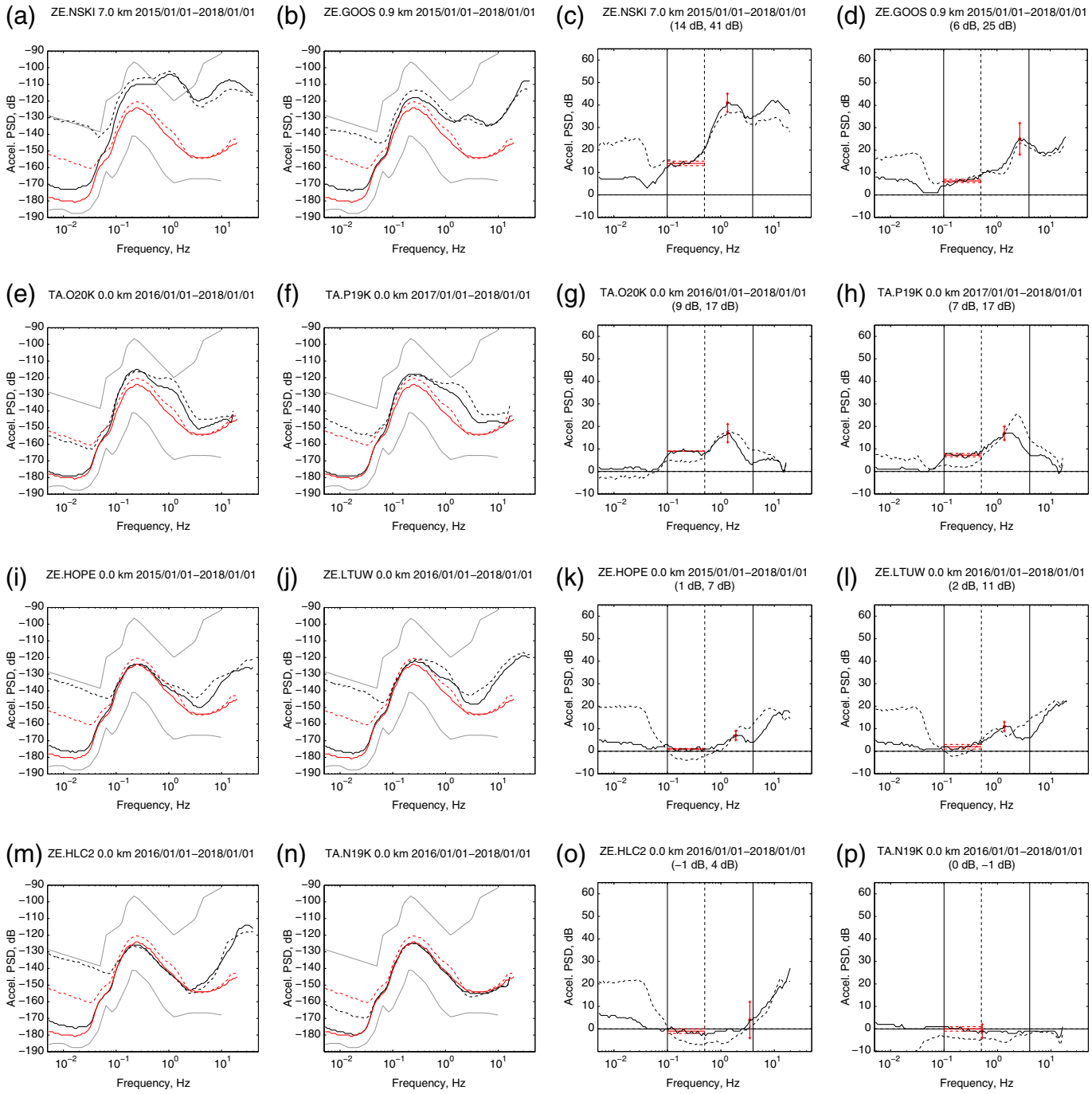

Figure 3. Annual ambient-noise spectra for eight stations in the Cook Inlet region. The solid spectra are for the vertical component; the dashed spectra are for the average of the two horizontal components. In each subplot, the red spectra are for the nonbasin reference station SSN. The gray spectra denote the new high-noise model (NHNM) and new low-noise model (NLNM) reference spectra (Peterson, 1993). (a,b) Basin stations NSKI and GOOS; (c) differential spectra for (a), which highlights the basin influence (and other differences); (d) differential spectra for (b); (e,f) basin-like marginal stations O20K and P19K; (g,h) differential spectra for (e,f); (i,j) marginal stations HOPE and LTUW; (k,l) differential spectra for (i,j); (m,n) nonbasin stations HLC2 and N19K; and (o,p) differential spectra for (m,n). The color version of this figure is available only in the electronic edition.

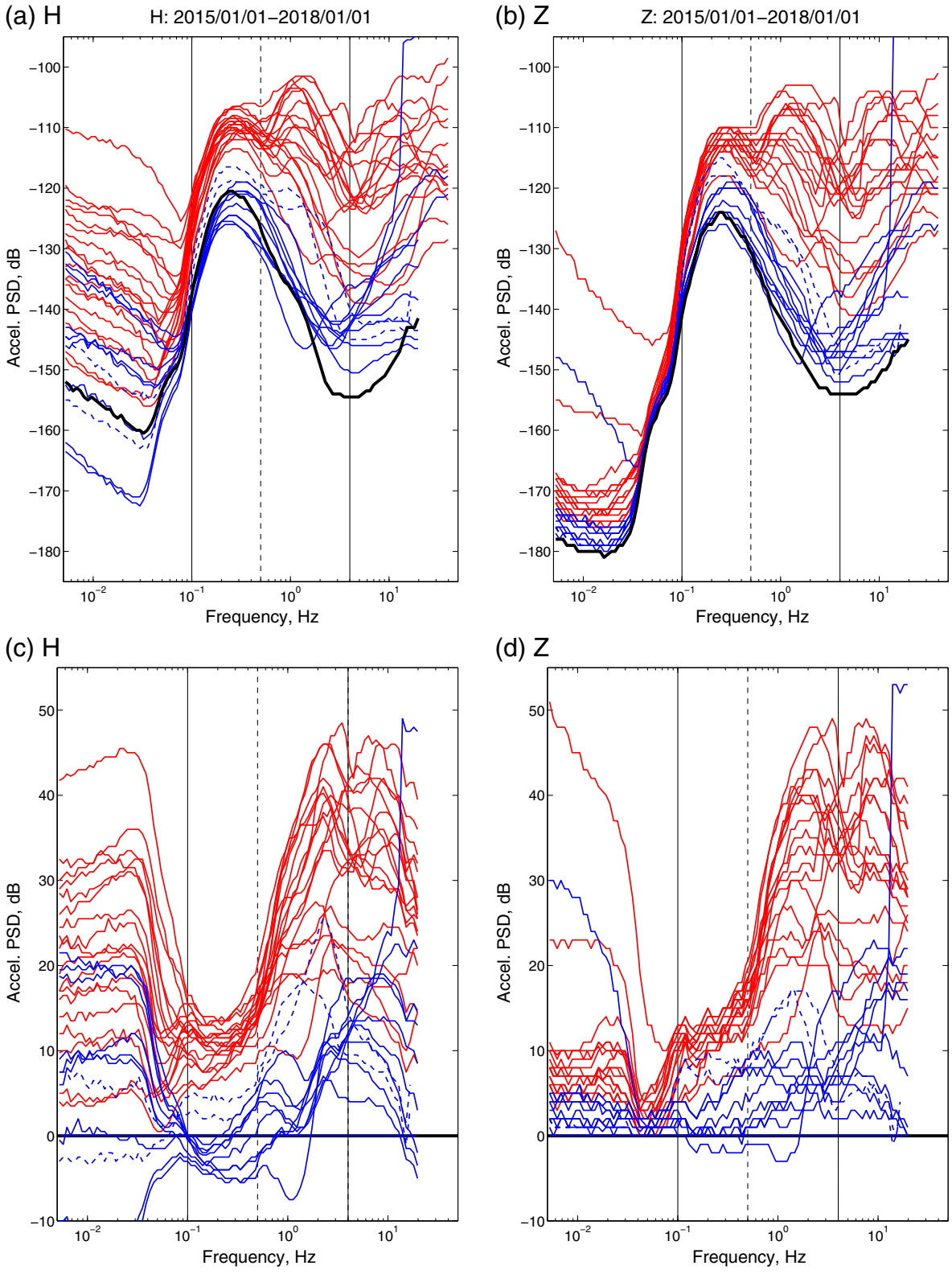

Figure 4. Seismic noise spectra and their differences from a nonbasin reference station (SSN). (a) Horizontal-component annual ambient noise for 30 stations in the Cook Inlet region. Red spectra are for 18 basin stations. Dashed blue spectra are for marginal basin stations (P19K and O20K) that exhibit basin-like characteristics. Solid blue spectra are for nine marginal basin stations that exhibit nonbasin characteristics. The thick black line is the nonbasin reference spectrum SSN. Solid lines denote the frequency range of basin influence on seismic waves: 0.1–4.0 Hz (separated at 0.5 Hz). (b) Same as (a) but for the vertical component. (c) Spectra in (a) minus the nonbasin reference spectrum in (a). (d) Spectra in (b) minus the nonbasin reference spectrum in (b). The color version of this figure is available only in the electronic edition.

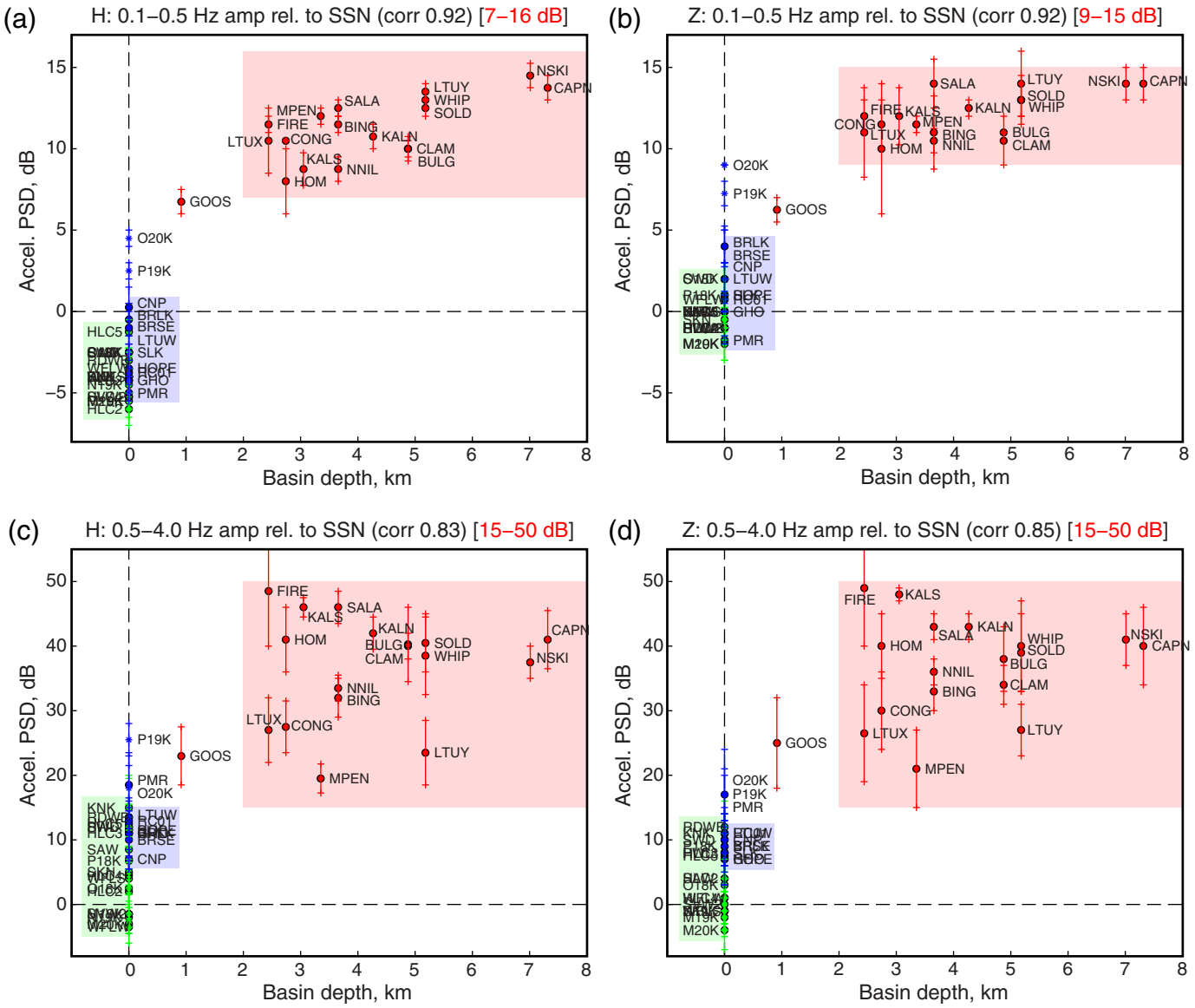

levels are within 3 dB of SSN (Fig. 5b). For the vertical component, the differences generally increase with distance from SSN (Fig. 5d), implying that there are either systematic subsurface structural differences from west to east or there are different sources generating the 0.5–4.0 Hz noise. For example, noise near Redoubt Volcano may be elevated (with respect to SSN) because of activity at the volcano, at glaciers, or in Cook Inlet, or it could be due to structural differences that affect the same background wavefield at both sites. Marginal stations (shaded blue in Fig. 5c,d) for the vertical component are mostly 8–16 dB higher than SSN. O20K and P19K both exhibit elevated noise levels, as do PMR, at the northeastern tip of the basin (in Palmer).

Figure 5. Seismic noise amplitudes compared with basin depth, shown for 48 stations in the Cook Inlet region. Red circles, highlighted by the red shaded region, denote 18 stations. Blue circles (and asterisks), highlighted by the blue shaded region, denote 12 marginal basin stations. (The asterisks are for P19K and O20K.) Green circles, highlighted by the green shaded region, are nonbasin stations. See Figure S2 (available in the supplemental material to this article) for individual spectra. (a) Horizontal-component seismic noise amplitudes for the frequency range 0.1–0.5 Hz. Note the *y*-axis limits from [–8, 17] dB. (b) Vertical component for 0.1–0.5 Hz. (c) Horizontal component for 0.5–4.0 Hz. Note the *y*-axis limits from [–8, 55] dB. (d) Vertical component for 0.5–4.0 Hz. The color version of this figure is available only in the electronic edition.

Ground-Motion Metrics Measured from Earthquakes

From a set of 34 earthquakes, we examine three-component filtered seismograms at 48 stations. From each filtered seismogram, we calculate five scalar ground-motion metrics:

1. duration (dur)
2. radiated energy (E_R)
3. peak ground displacement (PGD)
4. peak ground velocity (PGV)
5. peak ground acceleration (PGA).

Using basin depths of Shellenbaum *et al.* (2010), we test the hypothesis that these quantities increase with basin depth at each station.

Our approach carries several assumptions. First, we do not know the exact relationship between basin depth and the five metrics. Therefore, a correlation coefficient between basin depth and a calculated metric, for a set of stations for one event, may not be appropriate. Second, the ground-motion metrics are based on amplitudes, which vary strongly at stations according to a station's azimuth relative to the earthquake source mechanism. Third, there are structural variations such as 3D heterogeneity—elastic or anelastic structure—that impact the recorded wavefield. Our approach assumes that the depth of the basin is the only structural factor influencing the ground-motion metrics.

Methods

Our methods for calculating and analyzing ground-motion metrics are as follows:

1. Using ObsPy (Beyreuther *et al.*, 2010; Krischer *et al.*, 2015), fetch seismograms from IRIS Data Management Center and then remove instrument response. Using the source and station coordinates (and the sensor angles), rotate to radial and transverse component. The result is a set of three-component velocity seismograms (units m/s).
2. Loop over a large set of band-pass filters. For each set of filtered seismograms:

   a. calculate signal-to-noise ratio (SNR) as $\max(|v(t)|)$ over the first 400 s after the origin time, divided by the maximum over the 100 s prior to the origin time. Exclude stations with SNR < 4;
   b. proceed if there are ≥ 4 stations with basin depths >1 km;
   c. apply a distance-based correction for geometric spreading (each correction will depend on the band-pass via the filtered seismograms used); and
   d. calculate correlation coefficient between basin depth and a particular metric (e.g., PGV).

3. Generate a colored plot of correlation coefficients.These methods are demonstrated in Figures 6–8. The example earthquake is northeast of Cook Inlet basin, depth 12 km, M_L 4.1, on 2016-11-06. A map in Figure S9a shows the epicenter and the subset of 46 (out of 48) stations that recorded the earthquake. An unfiltered record section of transverse component is shown in Figure S9b.

We choose frequency limits for band-pass filters by $\mathbf{f} = 10^{\text{linspace}(\log_{10} f_{\min}, \log_{10} f_{\max}, n)}$, in which linspace$(x, y, n)$ returns a set of n linearly spaced values between x and y. With $f_{\min} = 0.10$ Hz, $f_{\max} = 4.00$, and $n = 8$, the frequencies are

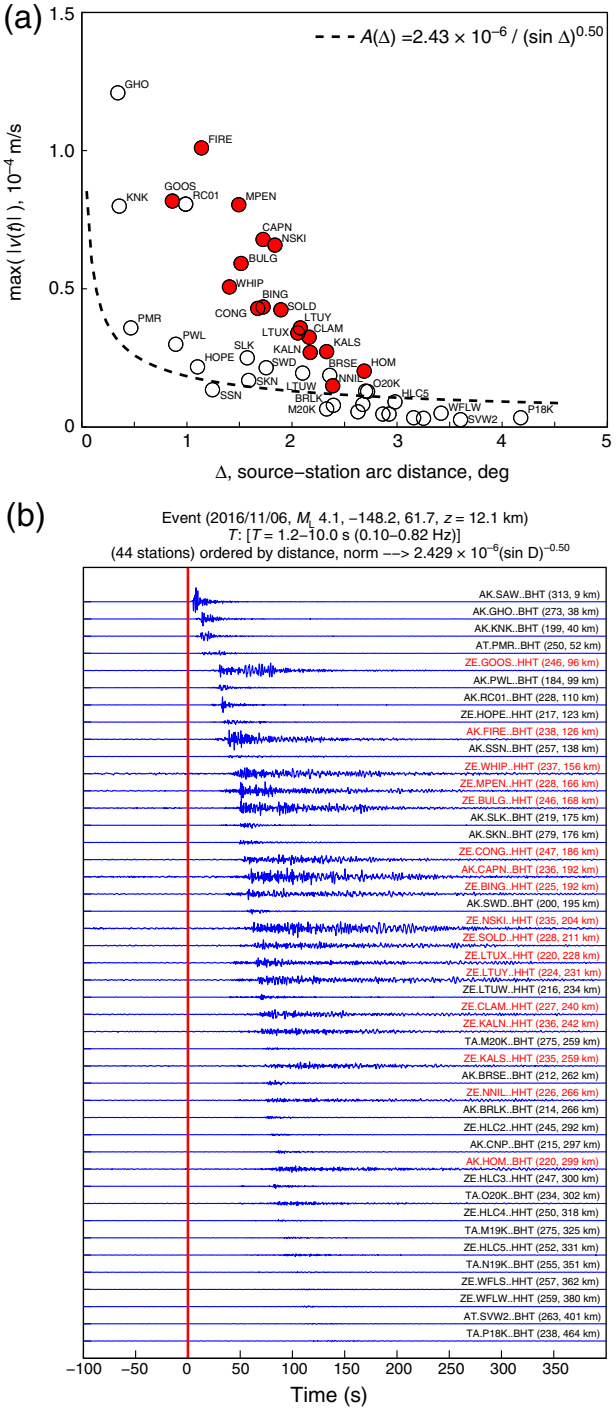

Figure 6. Distance-dependent correction for geometrical spreading. A full set of explanatory figures for earthquake metrics is shown in Figures 6–8. (a) Maximum absolute-value amplitudes of seismograms (in this case, transverse component) plotted as a function of epicentral distance Δ. The best-fitting curve is estimated using 26 nonbasin and marginal basin stations whose seismograms exceed our signal-to-noise criteria. The closest station AK.SAW is not shown because its value exceeds the plotting scale. (b) Record section filtered 0.10–0.82 Hz and corrected for geometrical spreading. Stations are sorted from top to bottom by increasing epicentral distance. The uncorrected record section is shown in Figure S9. The color version of this figure is available only in the electronic edition.

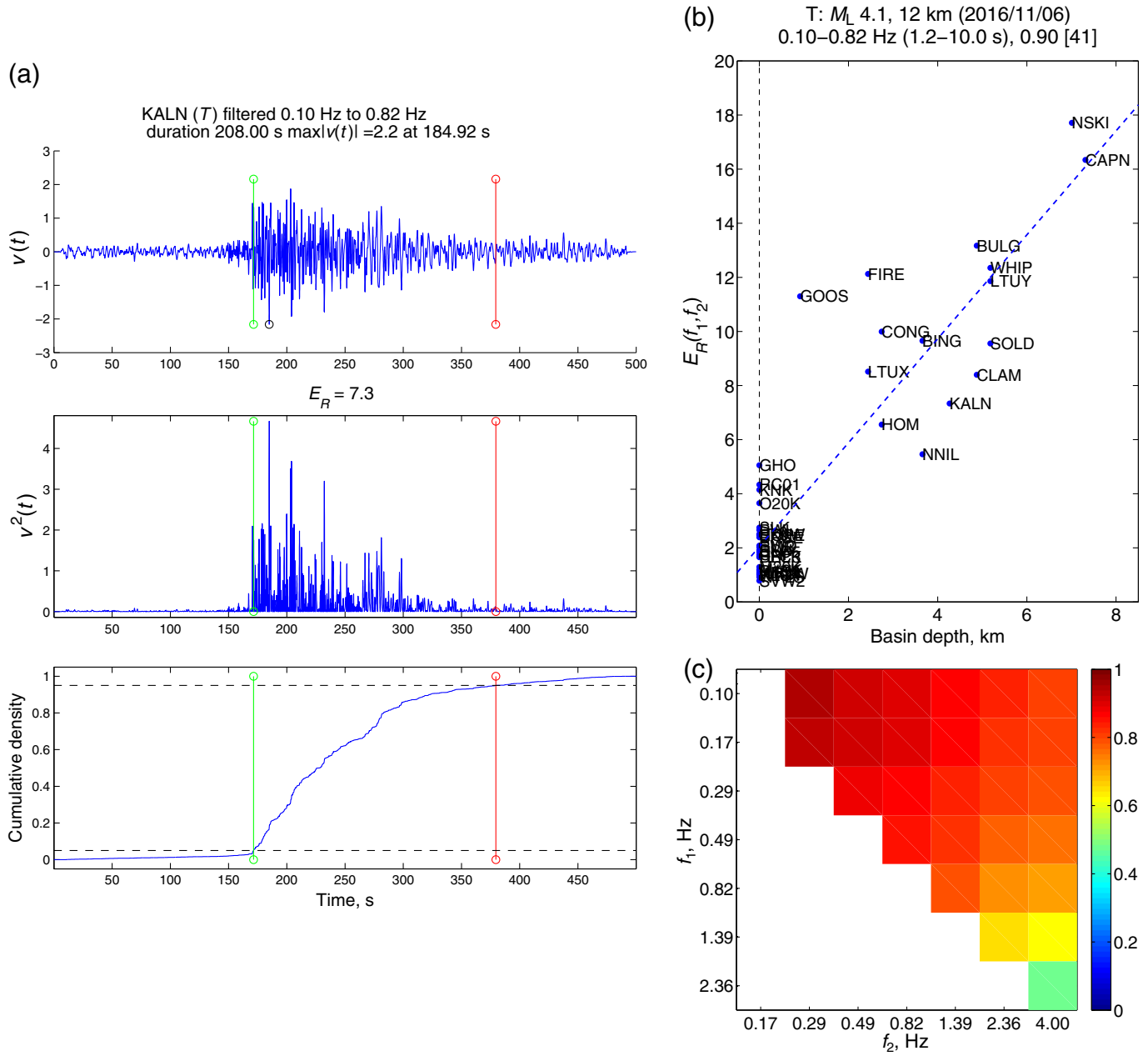

Figure 7. Construction of a matrix plot (c) from filtered seismograms. (a) Example calculation of metrics (dur, E_R) for a seismogram (KALN, T component, 0.10–0.82 Hz) from Figure 6b. Vertical lines denote the estimated start (t_1) and end (t_2) times for the duration, which are determined from the bottom plot. (Top) Velocity seismogram; (middle) squared waveform. The value of $E_R = 7.3$ is the integration of $v^2(t)$ between t_1 and t_2. (Bottom) Cumulative squared waveform, normalized by E_R. Horizontal dashed lines are values of 0.05 and 0.95 used to determine the seismogram duration. (b) Scatter plot between a seismogram metric (E_R) and basin depth. Station KALN, from (a), is plotted at 4.3 km and $E_R = 7.3$. The correlation coefficient is 0.90, and the number in square brackets is the number of stations used. (c) Matrix plot, which displays a colored correlation coefficient for each band pass [f_1, f_2] applied to a set of seismograms. The correlation coefficient of 0.90, from (b), is represented by the box on the top row and fourth column. This matrix plot appears in row 2, column 3 of Figure 8. The color version of this figure is available only in the electronic edition.

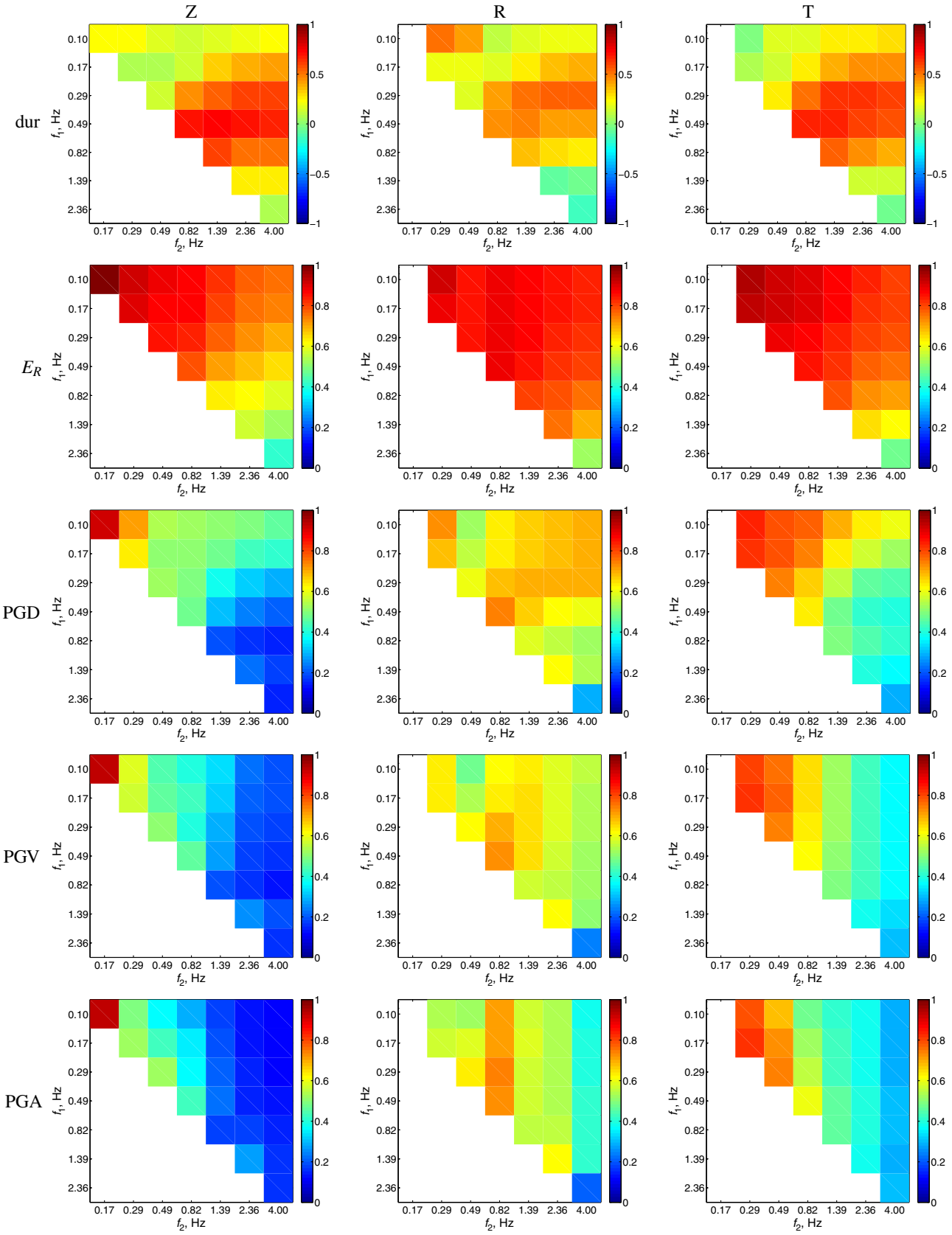

Figure 8. Matrix plots for earthquake metrics (dur, E_R, PGD, PGV, and PGA) for three components (R, radial; T, transverse; Z, vertical). The earthquake is M_L 4.1 on 2016-11-06 with depth 12 km event in the Cook Inlet region. A full set of explanatory figures for earthquake metrics is shown in Figures 6–8. Dur, duration; E_R, radiated energy; PGA, peak ground acceleration; PGD, peak ground displacement; PGV, peak ground velocity. The color version of this figure is available only in the electronic edition.

0.10, 0.17, 0.29, 0.49, 0.82, 1.39, 2.36, and 4.00 Hz. With n frequencies, we have a total set of $n(n-1)/2$ possible band-pass filters; therefore, there are 28 filters used for each set of seismograms. One filtered record section (0.10–0.82 Hz) is shown in Figure S9c. The record section excludes two stations (TA.O18K and TA.P19K) that do not meet the SNR threshold.

The next step is to correct the record section for geometrical spreading. We make the assumption that the seismograms are dominated by surface-wave energy. In this case, the amplitudes of the seismograms have a term $1/\sqrt{\sin\Delta}$, in which Δ is the arc distance from source to station (Stein and Wysession, 2003, Sec. 4.3.4, Eq. 20). (The same equation has a frequency-dependent attenuation term, which we ignore.) We correct for geometrical spreading of surface waves by estimating a single parameter

$$K = \text{median}(\max(|v_i(t)|)\sqrt{\sin\Delta_i}, \quad i = 1, \ldots, n), \tag{1}$$

in which i is the station index and n is the number of nonbasin stations with filtered seismograms passing the SNR threshold. The seismogram corrected for geometric spreading is then

$$v_i'(t) = \frac{\sqrt{\sin\Delta_i}}{K} v_i(t). \tag{2}$$

After normalizing by K, the seismogram is unitless. We estimate K for each record section of filtered waveforms and for each event. Figure 6 shows an example in which $K = 2.43 \times 10^{-6}$ m/s is calculated from a set of 26 nonbasin stations. Basin stations are excluded from estimating K because amplitudes of seismograms at basin stations are strongly influenced by basin structure. As expected, the best-fitting curve $K/\sqrt{\sin\Delta}$ offers a reasonable fit to nonbasin stations, and it does not explain the amplitude variations for the basin stations. The record section corrected for geometrical spreading is shown in Figure 6b.

From the filtered, distance-corrected seismograms in Figure 6b, we calculate five ground-motion metrics. An example calculation of dur, PGV, and E_R is shown in Figure 7a for station KALN, transverse component filtered 0.10–0.82 Hz. In this case, dur = 208.0 s, PGV = 2.2, and E_R = 7.3. These calculations are performed for each station's seismogram, and then the values are plotted versus basin depth at each station, as shown in Figure 7b for E_R. In this case, the data for basin depth and E_R have a correlation coefficient of 0.90.

We use a matrix plot of colored correlation coefficients—which we will call "matrix plots"—to represent the full set of different band-pass filters used. With n = 8 frequencies, there are 28 band-pass filters and therefore up to 28 colored boxes in matrix plots such as Figure 7c. The first band-pass considered is 0.10–0.17 Hz (5.90–10.00 s); for the event in Figure 6, there are not enough stations with sufficient SNR, and therefore the uppermost left square of Figure 7c is left white. The next band-pass is 0.10–0.29 Hz (3.49–10.00 s), which happens to provide the highest correlation between basin depth and E_R, among all 28 band passes. This is represented by the dark red box in row 1, column 2 of Figure 7c, with the corresponding scatter plot in Figure 9. The example in Figure 7b, for band-pass 0.10–0.82 Hz, corresponds to row 1, column 4 of Figure 7c. The matrix plot boxes along the diagonal represent narrowband filters (0.10–0.17 Hz, 0.17–0.29 Hz, 0.29–0.49 Hz, and so on), and the boxes at the far right represent broadband filters (0.10–4.00 Hz, 0.17–4.00 Hz, 0.29–4.00 Hz, and so on). The matrix plot therefore provides a compact representation of which band-pass filters lead to ground-motion metrics that are the best correlated with basin depths.

Results

The matrix plot in Figure 7c is one of 15 subplots in Figure 8. Each matrix plot is made from 28 possible scatter plots, and Figure 9 displays the scatter plot having the highest correlation coefficient. A full set of plots such as Figures 8 and 9 is included in Smith (2019) for 34 earthquakes. Here, we discuss the results for two earthquakes: an M_L 4.1 crustal event (12 km) on 2016-11-06 (Figs. 8 and 9) and an M_L 5.2 intraslab event (126 km) on 2015-07-25 (Figs. 10 and 11).

The ground-motion metric E_R combines duration and amplitude because it is an integration over time. Therefore if there are high correlations between peak amplitudes (PGD, PGV, and PGA) and basin depth, we would expect to see correlations between E_R and basin depth. Similarly, if durations correlate with basin depth, we would expect to see correlations between E_R and basin depth.

For the crustal earthquake, there are <10 basin stations that exceed the SNR threshold for the lowest frequency band-pass (0.10–0.17 Hz, 5.90–10.00 s) for the vertical component. These stations produce correlation coefficients of 0.90–0.99, as indicated by the Z column of plots in Figure 9. Interestingly, for the same band pass, the correlation between duration and basin depth is weak, indicated by the lack of red color in the upper left matrix plot in Figure 8. For the vertical and transverse components, duration correlates with basin depth at 0.49–1.39 Hz, yet there is large scatter even for nonbasin stations (Fig. 9, top row).

Similar to the crustal event, the intraslab event exhibits the highest (and most) correlations from E_R (Fig. 10). Although this event is deeper from the crustal event, its magnitude is sufficiently greater (5.2 vs. 4.1) such that its seismograms have overall higher SNR and more data points appear in the scatter plots (Fig. 11). Cross correlation coefficients (cc) between duration and basin depth are highest on the vertical component and for 0.29–0.82 Hz (cc 0.86). The biggest outliers in the (dur, Z) scatter plot in Figure 11 are the two basin-like stations O20K and P19K; they would not be outliers if they were assigned greater basin depths. For the other four metrics (E_R, PGD, PGV, and PGA), there are much higher correlations with basin depth for horizontal components than for the vertical component

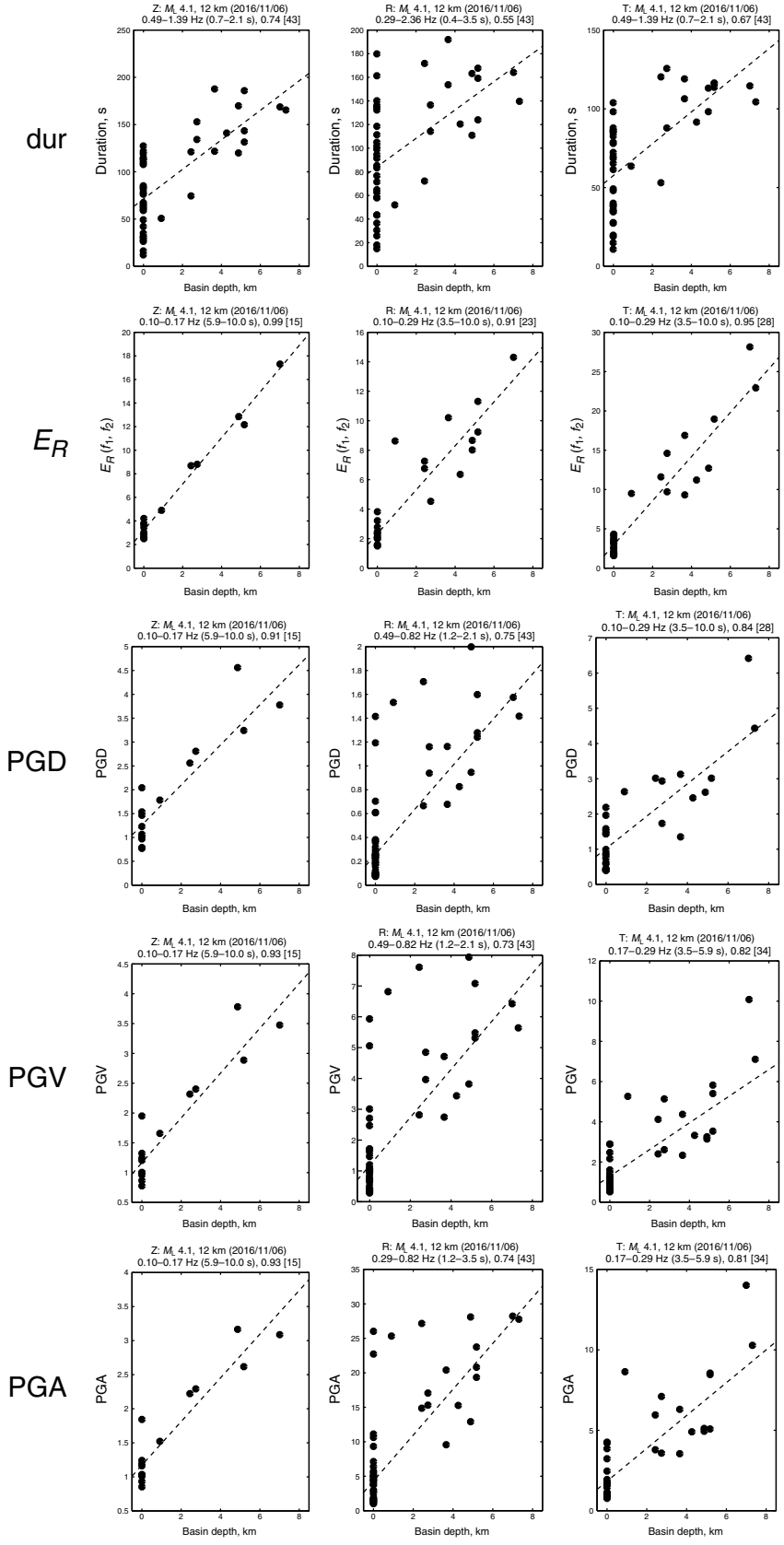

Figure 9. Scatter plots corresponding to the highest correlation coefficients in each of the 15 matrix plots in Figure 8. The band-pass filter may be different for each subplot. This may also affect the number of data points used, which is determined by the number of filtered seismic waveforms that exceed our signal-to-noise threshold.

(Fig. 10). Correlations exceed 0.90 for the transverse component for the frequency range 0.17–0.49 Hz (2.06–5.90 s). Further work is needed to examine the influence of the source mechanism and the geometry of the basin on these results.

Based on the full set of band-pass filters for the full set of 34 earthquakes in Smith (2019), we provide some summary points regarding correlation coefficients between ground-motion metrics and basin depth. (1) Among the five ground-motion metrics, E_R, which combines duration and amplitudes, has the highest correlations with basin depth. (2) PGD, PGV, and PGA have similar correlations with basin depth. This is not surprising because a sinusoidal wave $d(t) = F \sin t$ would lead to PGD $= F$, PGV $= F$, and PGA $= F$. (3) For PGD, PGV, and PGA, correlations with basin depth are higher for R and T components than for Z.

Spectral Ratios Measured from Earthquakes

Methods

Using the same set of 34 earthquakes and 48 stations, we calculate spectral ratios (SRs) between each target station and a nonbasin reference station. At this initial stage, we do not account for amplitude differences that would arise from (1) different epicentral distances for the target station and the reference station, (2) different source–station azimuths that would result in different amplitudes with respect to the source mechanism, or (3) different local structure at two stations (TA.O20K and TA.P19K) that would affect the recorded

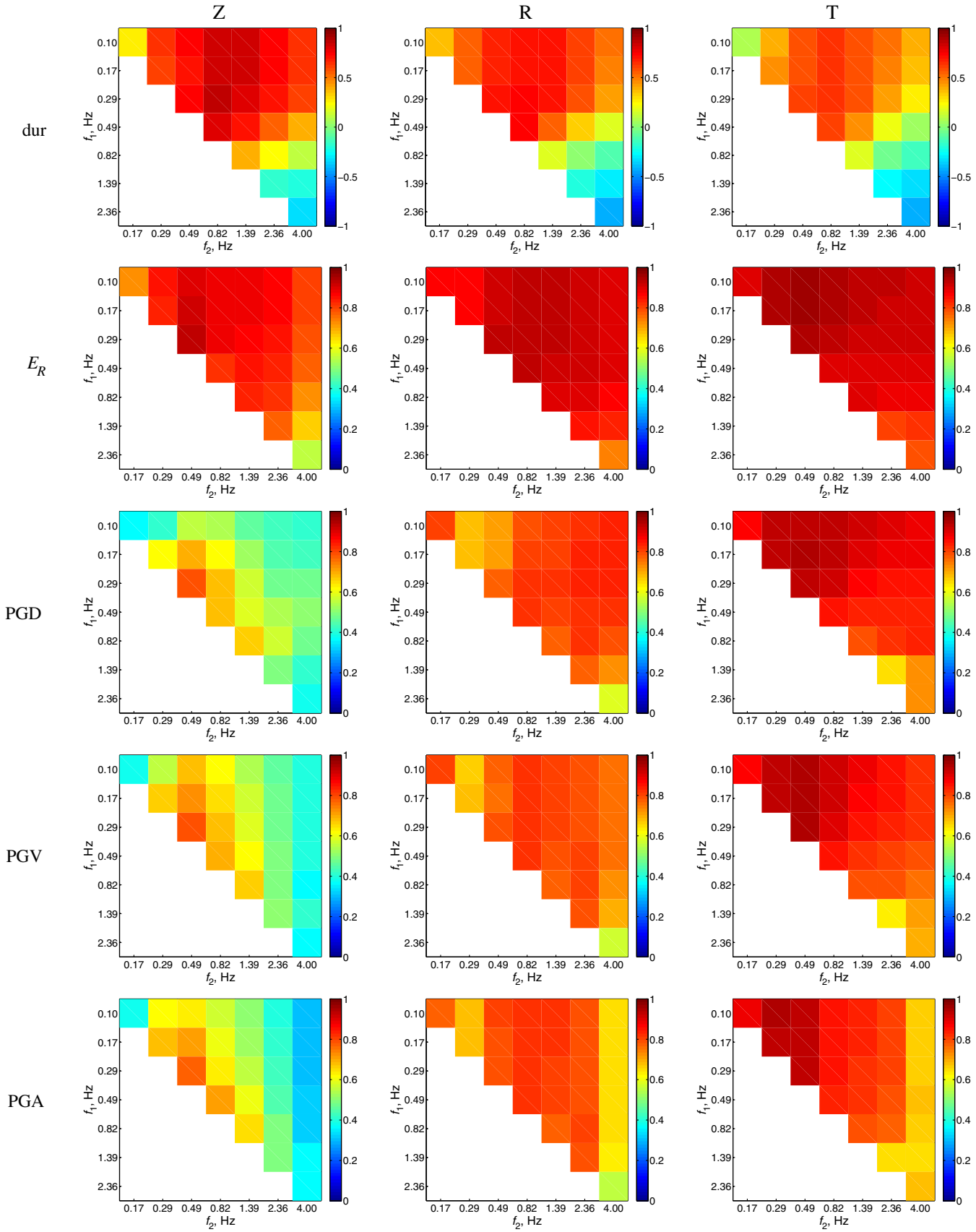

Figure 10. Matrix plots for earthquake metrics (dur, E_R, PGD, PGV, and PGA) for three components (R, radial; T, transverse; Z, vertical). The earthquake is M_L 5.2 on 2015-07-25 with depth 126 km event in the Cook Inlet region. The color version of this figure is available only in the electronic edition.

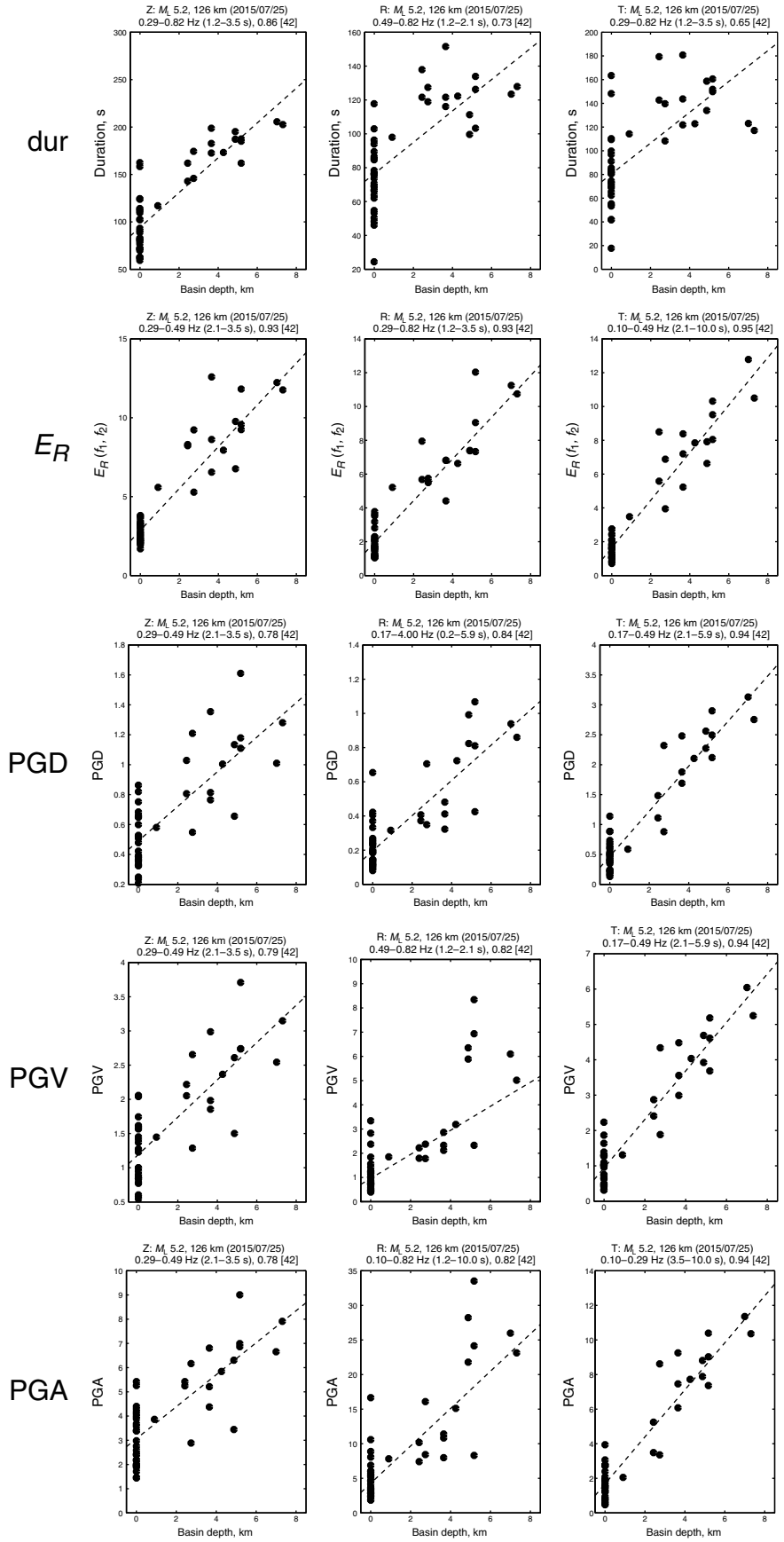

Figure 11. Scatter plots corresponding to the highest correlation coefficients in each of the 15 matrix plots in Figure 10.

wavefield. We partially address (1) and (3) by grouping the stations into three subregions and assigning a different reference station for each subregion. West of Cook Inlet, we use TA.N19K; north of Cook Inlet, we use AK.SSN; and east of Cook Inlet, we use AK.SLK (Fig. 1a). The reference station for each target station is listed in Table S2. The three primary reference stations are not used as target stations; therefore, we have 45 (of 48) target stations for the analysis.

Our goal is to calculate scalar quantities from the SR between a target station and a nonbasin reference station. These scalar quantities are the median acceleration power over two frequency intervals: 0.1–0.5 Hz and 0.5–4.0 Hz. Our assumption is that basin effects are confined to 0.1–4.0 Hz. Our procedure is demonstrated in Figure 12 for target station NSKI and reference station SLK. For both stations, for the "signal" we select a time window of 500 s following the origin time; for the "noise," we select a time window of 500 s before the origin time. We calculate acceleration power spectra following the procedures of McNamara and Buland (2004), but with less smoothing (1/8 octave instead of full octave). Four spectra—signal and noise for both stations—are shown in Figure 12a.

The signal and noise spectra are used to refine the two frequency intervals over which the SR measurements are made. For the earthquake in Figure 12, NSKI meets the SNR criterion at 0.97 Hz, whereas SLK meets the criterion at 0.52 Hz. Therefore, for the low-frequency interval (0.1–0.5 Hz), there is

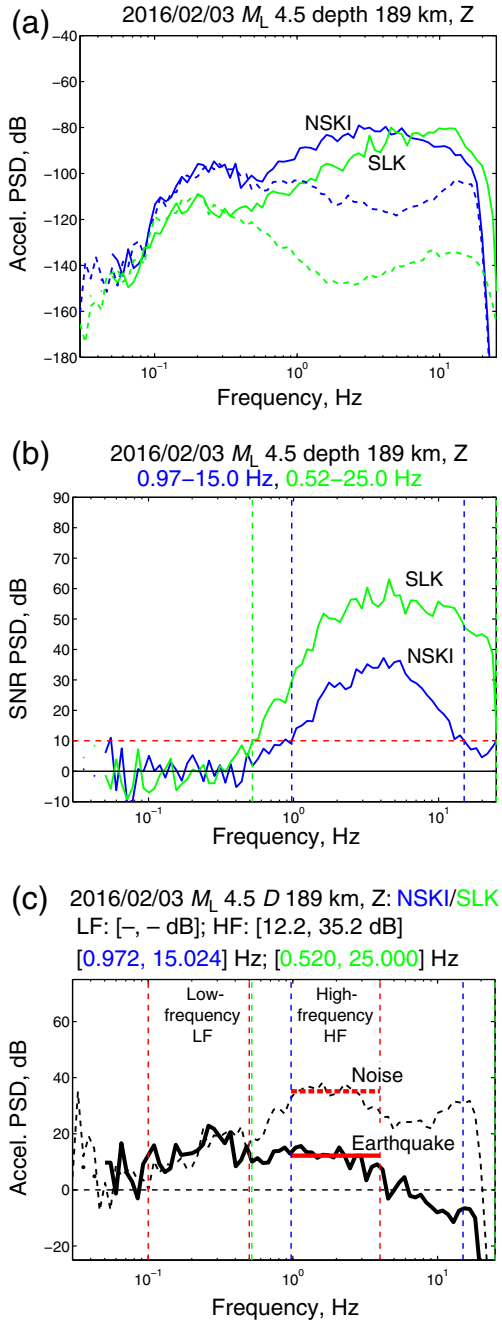

Figure 12. Example calculation of a spectral ratio (SR) for station NSKI, with respect to SLK, for an M_L 4.5 earthquake on 2016-02-03 at a depth of 189 km. The frequency range shown is between 0.03 and 25 Hz. (a) Acceleration power spectra. Solid-line earthquake spectra are calculated from the 500 s following the origin time of the earthquake for target station NSKI and for reference station SLK. Dashed-line noise spectra are calculated from the 500 s prior to the origin time. (b) Signal-to-noise ratios (SNRs) calculated by subtraction (in log space) of the dashed-line spectra in (a) from the solid-line spectra. (c) SRs between two stations, shown for an earthquake (solid) and for pre-earthquake noise (dashed). Vertical red dashed lines denote two intervals (0.1–0.5 Hz and 0.5–4.0 Hz) over which median measurements of the SR are made if the earthquake signal exceeds noise levels (b). The color version of this figure is available only in the electronic edition.

insufficient signal to calculate an SR. For the high-frequency interval (0.5–4.0 Hz), the lower limit of 0.5 Hz is increased to 0.97 Hz. Over this interval (0.97–4.0 Hz), the measurement is 12 dB, which corresponds to an amplification factor of ~4 (Table S1). The SR for noise is much larger (35 dB) than for earthquakes, something we find across most events and station pairs (Smith, 2019).

This procedure is repeated for all 34 earthquakes recorded by the target station, as shown in Figure 13. From this set of SR measurements, we calculate the median value and enter it into Table S2. This process is performed for each station, for three components, and for two frequency intervals to complete Table S2.

Results

Our SR results are summarized in Table S2 and Figure 14a,b. We find that the median SRs for 0.1–0.5 Hz for all 18 are positive and range from 6 to 14 dB. Furthermore, the two basin-like marginal stations (TA.O20K and TA.P19K) have ratios of 5–7 dB (Fig. 14a), further evidence that these stations should be characterized as basin stations. For 0.5–4.0 Hz SRs (Fig. 14b), there is a similar pattern of elevated values for basin stations, but the variability—even for nonbasin stations—is large.

The scatter in the SR measurements is partially the result of geometric spreading not being included within our simplified approach. For any earthquake, the epicentral distances to the target station (Δ_{tar}) and reference station (Δ_{ref}) will be different. We calculate $\Delta D = \Delta_{ref} - \Delta_{tar}$ for all source–station pairs to identify the stations that would be most affected by ignoring the distance effect. Target stations whose mean value $\Delta D > 50$ km are generally farther from earthquakes than is the reference station; this list includes basin station HOM as well as nonbasin stations M19K, SAW, CNP, P18K, M20K, GHO, BRSE, BRLK, KNK, O18K, SVW2, and PMR. These stations are colored blue in Figure 14a and tend to have lower decibel values than other stations with similar basin depths. Target stations whose mean value $\Delta D < 50$ km are generally closer to earthquakes than is the reference station; this list includes basin stations KALS and KALN as well as nonbasin stations O20K, RDWB, HLC2, and HLC3. These stations are colored black in Figure 14a,b and tend to have higher decibel values than other stations with similar basin depths. Careful treatment of the distance effect, as well as of source mechanisms, would allow for a better examination of any possible relationship between basin depth and amplification. This is particularly important for the high-frequency band pass (0.5–4.0 Hz).

Discussion

The use of broadband seismometers allows us to examine how the seismic wavefield interacts with Cook Inlet sedimentary basin across a wide range of frequencies (0.01–40 Hz). Our three analyses examined frequency-dependent effects using ambient noise (no sources), ground-motion metrics (1 source,

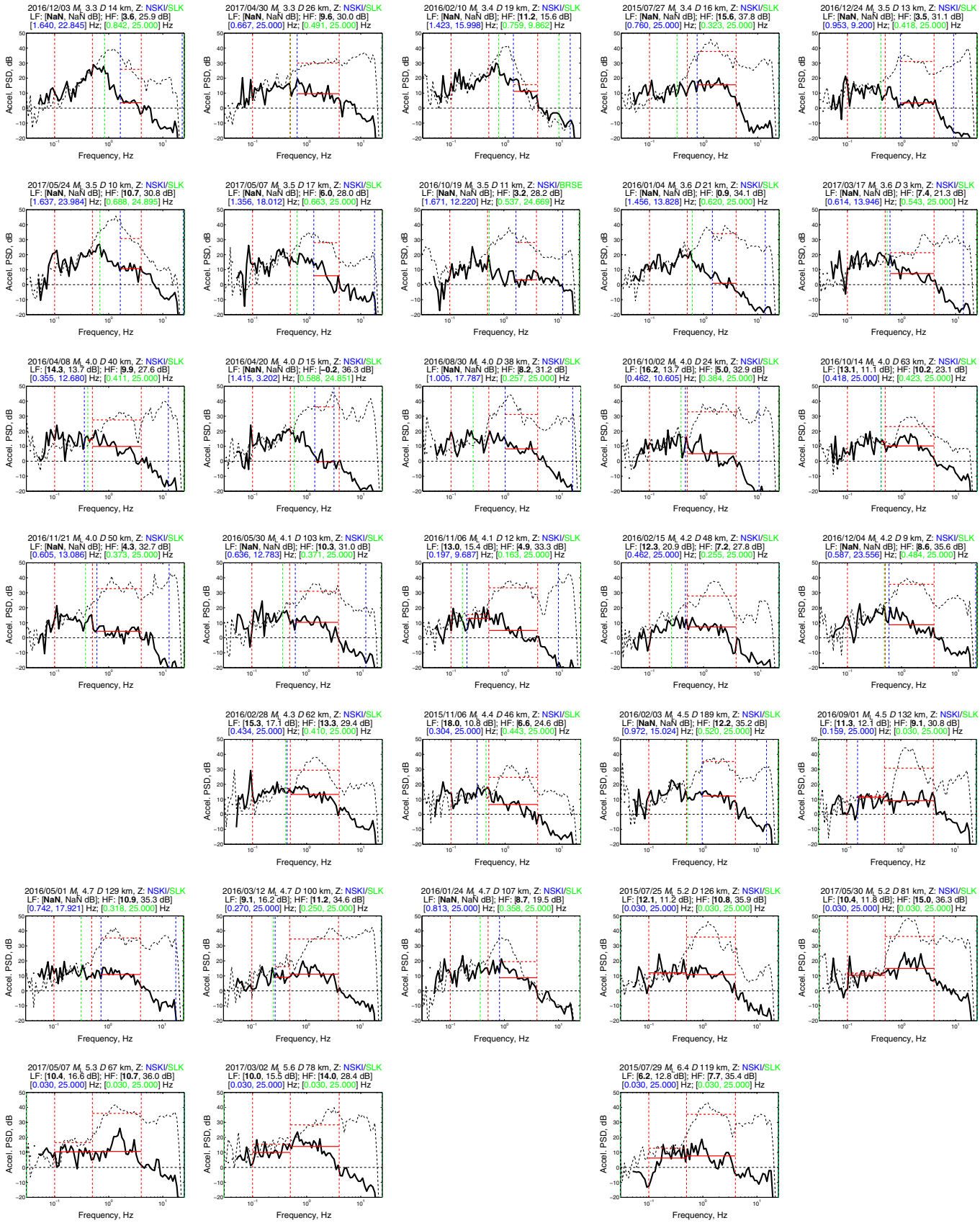

Figure 13. SRs between station NSKI (basin depth 7.0 km) and nonbasin reference station SLK for a subset of 32/34 earthquakes sorted by increasing magnitude. The solid-line SR spectrum is for the earthquake; the dashed-line SR spectrum is for pre-earthquake noise. See Figure 12c for details. The color version of this figure is available only in the electronic edition.

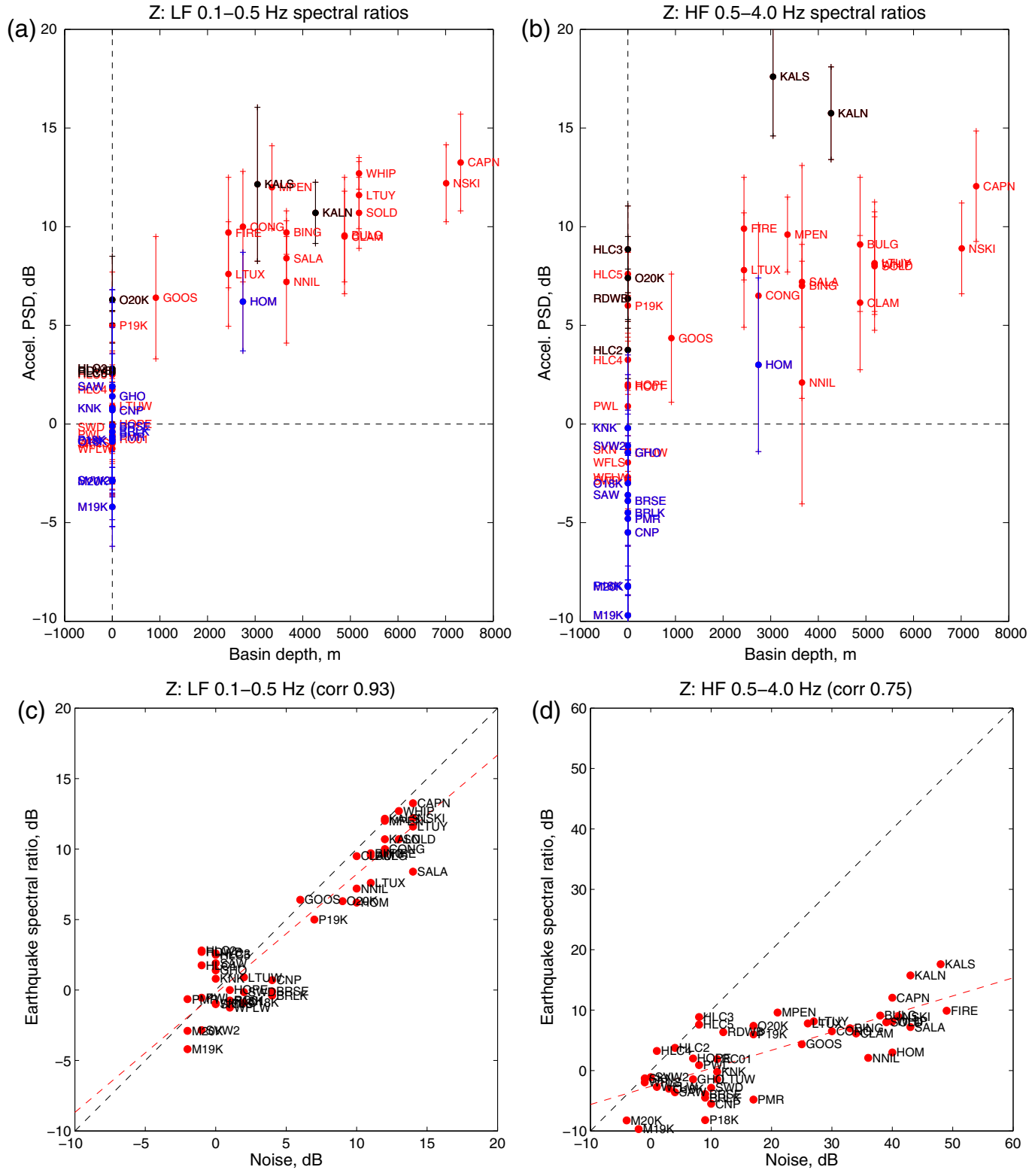

Figure 14. Summary of SR results for 45 seismic stations in the Cook Inlet region. (a) SRs for vertical component, 0.1–0.5 Hz. Each data point and error bar is derived from SRs at one station for up to 34 earthquakes (see Table S2); an example for one station is shown in Figure 13. The points are colored to highlight the influence of different distances from stations to events. See Figure S10 for results for the radial and transverse components. (b) Same as (a) but for the high-frequency band pass (0.5–4.0 Hz). (c) Comparison between vertical-component seismic power from earthquakes and from noise, calculated for the vertical component for 0.1–0.5 Hz. The noise values, on the *x* axis, are from Figure 4b. The earthquake SRs, on the *y* axis, are from (a). (d) Same as (c) but for the high-frequency band pass (0.5–4.0 Hz). The noise and earthquake data are in general agreement for 0.1–0.5 Hz but not for 0.5–4.0 Hz. The color version of this figure is available only in the electronic edition.

all stations), and SRs (one station, all sources). Next, we generalize our results and discuss some unresolved topics.

The seismic wavefield from earthquakes and ambient noise

Results from ground-motion metrics and from SRs indicate that the seismic wavefield from crustal and intraslab earthquakes is amplified by Cook Inlet basin. In the case of the ground-motion metrics, the stations in the deeper basin exhibit higher amplitudes than stations at the margin or outside of the basin. SRs provide an opportunity to compare noise as well as signal for pairs of stations. An example for a single station is shown in Figure 13 for basin station NSKI. For the largest events such as the five that have $M_L > 5$, the earthquake signal exceeds the pre-earthquake noise level, even down to 0.1 Hz. The calculated SRs for 0.1–0.5 Hz are all ~10 dB, corresponding to an amplification factor of about 3. The pre-earthquake noise SRs have similar values. However for higher frequencies (0.5–4.0 Hz), the peak noise SRs increase to 40–50 dB, similar to the values obtained when examining 2 yr of continuously recorded ambient noise (Fig. 5d).

The divergence above 0.5 Hz between earthquake SRs and noise SRs is highlighted between Figure 14c and 14d. This suggests that the same wavefield (earthquake or ambient noise) is not being measured at both the target basin station and the reference nonbasin station. Rather than interpreting the 40 dB noise SR at 0.5–4.0 Hz (Fig. 4d) as "basin amplification" of the same waves comprising ambient noise, we can interpret that there are two different noise settings. With this interpretation, the waves comprising the ambient noise in the basin do not reach the nonbasin reference station.

Analysis of seismic noise ratios—whether from 500 s of pre-earthquake noise or from 2 yr of continuous data—suggests that surface waves at 0.1–0.5 Hz, either from earthquakes or within ambient noise, are amplified in Cook Inlet basin by 6–14 dB.

Improvements to the assumed basin model

Our modeling and interpretations are based on the detailed basement map of Shellenbaum *et al.* (2010), which is estimated from well logs and stacking velocities (mostly *P* waves) from industry data. Future seismic modeling with SALMON and other data may allow for improvements of the basement surface, the internal basin wavespeed structure, and the underlying structure. An optimal approach would be to perform tomographic inversion using the full seismic waveforms (earthquakes and ambient-noise cross correlations) and allowing for perturbations of the boundary surface in addition to the wavespeed structure (Dahlen, 2005; Tong *et al.*, 2014).

Our analysis of low-frequency (0.1–0.5 Hz) noise provides some indication of corrections needed to the assumed basin geometry. The variations in the marginal basin differential spectra (blue) in Figure 4 are likely due to differences either in the basement surface or the subsurface wavespeed structure. Two marginal stations in our analysis TA.O20K and TA.P19K have low-frequency noise levels that fall between basin stations and marginal stations (Fig. 4). The geological unit at the surface at these two stations is mapped as the Upper Jurassic Naknek Formation and Kotsina Conglomerate, which are interpreted to underlie the Tertiary Cook Inlet basin (Fisher and Magoon, 1978). One interpretation is that the 0.1–0.5 Hz ambient-noise wavefield at bedrock stations TA.O20K and TA.P19K is sensitive to basin structures that are up to 20 km east of the stations and within Cook Inlet basin. Alternatively, it is possible that the Naknek formation is anomalously slow and thick. This would imply that the Mesozoic strata—beneath the basement surface of Shellenbaum *et al.* (2010)—would be beneficial for modeling the seismic noise variations.

Intraslab bias from earthquake selection

Our results reveal basin influences down to 0.1 Hz. These frequencies are best excited by larger ($M_L > 5$) earthquakes, which, in our study region, are all intraslab earthquakes. Two notable historical crustal earthquakes have occurred in this region: the 1933-04-27 M_w 6.8 and 1943-11-03 M_w 7.3 earthquakes (Doser and Brown, 2001; Silwal *et al.*, 2018). Neither of these earthquakes is associated with an actively mapped fault (Koehler *et al.*, 2012). (The 1933 earthquake is within a region mapped as actively folding sub-basin structures; Haeussler *et al.*, 2000.)

With regard to basin excitation, it is important to acknowledge that our results are biased toward the intraslab earthquakes that were recorded during the SALMON deployment. Intraslab earthquakes of a given magnitude will not excite surface waves as strongly as a shallow crustal earthquake; furthermore, the incident angle of the arriving wavefield will differ. Any future modeling of ground motions for the sake of seismic hazard estimates should take into account the possibility of crustal earthquakes from realistic (e.g., historical) source regions.

Attenuation and source radiation effects

Our treatment of modeling seismic amplitudes is overly simplified and should be revised in a future analysis of this data set. A distance correction for geometrical spreading was used in the analysis of ground-motion metrics but not in the analysis of SRs. Furthermore, our treatment of geometrical spreading assumes the dominance of surface waves, which may not be appropriate at higher frequencies and does not account for the influence of source depth (Wirth *et al.*, 2019). Attenuation (anelasticity) was not considered. Attenuation of surface waves is encapsulated with the term $\exp[\tau\pi f/\mathrm{Q}]$, in which $\tau = a\Delta/U$ is the travel time, Δ is the arc distance, a is the Earth's radius, and U is the group velocity (Stein and Wysession, 2003, Sec. 4.3.4, Eq. 20). High values of Q correspond to a slow decay of amplitudes of seismic waves (low attenuation).

Source radiation has a strong influence on amplitudes of surface waves and body waves. The data coverage for all 34 earthquakes in this study should be sufficient to obtain reliable source mechanisms (Silwal and Tape, 2016; Silwal *et al.*, 2018). Incorporating the amplitude variation expected at each station for each event would improve our estimates of the influence of basin depth on amplitudes.

Summary

Our main findings are as follows:

1. We analyze 34 earthquakes between 2015-05-01 and 2017-08-01 recorded by 48 stations. The time period spans the SALMON project (Tape *et al.*, 2017), which offers the best spatial coverage of Cook Inlet basin, including stations on the west side of Cook Inlet.
   Most of the larger earthquakes are intraslab events below 50 km depth. No large ($M_w > 5$) crustal events, which are known to occur in the region (e.g., 1933-04-27 M_w 6.8 in Cook Inlet; Doser and Brown, 2001; Silwal *et al.*, 2018), occurred during the SALMON deployment.
2. Earthquake SRs between basin and nonbasin stations imply basin amplification of 6–14 dB for 0.1–0.5 Hz.
3. Correlations between basin depth and ground-motion metrics depend on the component of ground motion. Amplitude-based ground-motion metrics (E_R, PGD, PGV, and PGA) are generally higher for the horizontal component of ground motion than for the vertical component. For larger earthquakes, the correlations between basin depth and duration are higher for the vertical component than for the horizontal component.
4. Cook Inlet basin exhibits vertical-component ambient seismic noise that is amplified relative to a nonbasin reference site by 9–15 dB at 0.1–0.5 Hz and 15–50 dB at 0.5–4.0 Hz. Similar amplification occurs for the horizontal component of noise.
5. The noise results at 0.1–0.5 Hz are in agreement with SRs, suggesting that the low-frequency earthquake wavefield and ambient-noise wavefield are similarly amplified by Cook Inlet basin.
6. The noise results at 0.5–4.0 Hz are not in agreement with the earthquake SRs, even for crustal earthquakes, suggesting that the high-frequency noise wavefield is local to the basin.

Future efforts dedicated to understanding seismic wave propagation in Cook Inlet basin should be possible from analysis of 3D seismic wavefield simulations and from improved modeling of the recorded earthquake waveforms. As our 3D models of elastic and anelastic structure improve in this region (Eberhart-Phillips *et al.*, 2006; Shellenbaum *et al.*, 2010; Ward and Lin, 2018), we will be able to design realistic numerical experiments (Day *et al.*, 2008; Cruz-Atienza *et al.*, 2016; Wirth *et al.*, 2019) to investigate the influence of Cook Inlet basin on the seismic wavefield, by isolating the roles of source location, source depth, source radiation, 3D attenuation, and 3D structure.

Data and Resources

Seismic data holdings from all stations in this study are openly available from the Incorporated Research Institutions for Seismology (IRIS) Data Management Center. Stations are from the following networks: AK (Alaska Earthquake Center, University of Alaska Fairbanks, 1987), AT (National Oceanic and Atmospheric Administration [NOAA], 1967), AV (Alaska Volcano Observatory/U.S. Geological Survey [USGS], 1988), TA (IRIS, 2003), and ZE (Tape *et al.*, 2015). The supplemental material contains a table relating power levels in decibels to amplification ratios, a summary table of spectral ratios, a set of eight figures of ambient-noise spectra, and two additional figures.

Acknowledgments

The authors thank two anonymous reviewers for their constructive feedback, Morgan Moschetti for helpful discussions, and Kasey Aderhold for providing drill logs and photographs for EarthScope TA stations and TA-upgrade stations. The Southern Alaska Lithosphere and Mantle Observation Network (SALMON) seismic experiment was funded by the National Science Foundation under Grant Number EAR-1251971. The field component was led by Doug Christensen, Carl Tape, and Melissa M. Moore-Driskell.

References

Alaska Earthquake Center, University of Alaska Fairbanks (1987). Alaska Regional Network. International Federation of Digital Seismograph Networks, Other/Seismic Network, doi: 10.7914/SN/AK.

Alaska Volcano Observatory/U.S. Geological Survey (USGS) (1988). Alaska Volcano Observatory. International Federation of Digital Seismograph Networks, Other/Seismic Network, doi: 10.7914/SN/AV.

Anderson, J. G., P. Bodin, J. N. Brune, J. Prince, S. K. Singh, R. Quaas, and M. Onate (1986). Strong ground motion from the Michoacan, Mexico, earthquake, *Science* **233,** 1043–1049.

Bard, P.-Y., and M. Bouchon (1980). The seismic response of sediment-filled valleys. Part 1. The case of incident *SH* waves, *Bull. Seismol. Soc. Am.* **70,** no. 4, 1263–1286.

Bard, P.-Y., and M. Bouchon (1985). The two-dimensional resonance of sediment-filled valleys, *Bull. Seismol. Soc. Am.* **75,** no. 2, 519–541.

Bard, P.-Y., M. Campillo, F. J. Chávez-Garcia, and F. Sánchez-Sesma (1988). The Mexico earthquake of September 19, 1985—A theoretical investigation of large- and small-scale amplification effects in the Mexico City valley, *Earthq. Spectra* **4,** no. 3, 609–633.

Beyreuther, M., R. Barsch, L. Krischer, T. Megies, Y. Behr, and J. Wassermann (2010). ObsPy: A Python toolbox for seismology, *Seismol. Res. Lett.* **81,** no. 3, 530–533, doi: 10.1785/gssrl.81.3.530.

Bindi, D., S. Parolai, D. Cara, G. Di Giulio, G. Ferretti, L. Luzi, G. Monachesi, F. Pacor, and A. Rovelli (2009). Site amplifications observed in the Gubbio basin, central Italy: Hints for lateral propagation effects, *Bull. Seismol. Soc. Am.* **99,** no. 2A, 741–760, doi: 10.1785/0120080238.

Borcherdt, R. D. (1970). Effects of local geology on ground motion near San Francisco Bay, *Bull. Seismol. Soc. Am.* **60,** no. 1, 29–61.

Bowden, D. C., and V. C. Tsai (2017). Earthquake ground motion amplification for surface waves, *Geophys. Res. Lett.* **44,** 121–127, doi: 10.1002/2016GL071885.

Carder, D. S. (1963). The requirements of a high-sensitivity seismograph stations, *VESIAC State-of-the-Art Report 4410-63-X*, Acoustics and Seismic Laboratory, Institute of Science and Technology, University of Michigan, Ann Arbor, Michigan, 72 pp.

Casey, R., M. E. Templeton, G. Sharer, L. Keyson, B. R. Weertman, and T. Ahern (2018). Assuring the quality of IRIS data with MUSTANG, *Seismol. Res. Lett.* **89,** no. 2A, 630–639, doi: 10.1785/0220170191.

Choi, Y., J. P. Stewart, and R. W. Graves (2005). Empirical model for basin effects accounts for basin depth and source location, *Bull. Seismol. Soc. Am.* **95,** no. 4, 1412–1427, doi: 10.1785/0120040208.

Clift, P., and P. Vannucchi (2004). Controls on tectonic accretion versus erosion in subduction zones: Implications for the origin and recycling of the continental crust, *Rev. Geophys.* **42,** 1–31.

Cruz-Atienza, V. M., J. Tago, J. D. Sanabria-Gómez, E. Chaljub, V. Etienna, J. Virieux, and L. Quintanar (2016). Long duration of ground motion in the paradigmatic Valley of Mexico, *Sci. Rep.* **6,** 1–9, doi: 10.1038/srep38807.

Dahlen, F. A. (2005). Finite-frequency sensitivity kernels for boundary topography perturbations, *Geophys. J. Int.* **162,** 525–540, doi: 10.1111/j.1365-246X.2005.02682.x.

Day, S. M., R. Graves, J. Bielak, D. Dreger, S. Larsen, K. B. Olsen, A. Pitarka, and L. Ramirez-Guzman (2008). Model for basin effects on long-period response spectra in southern California, *Earthq. Spectra* **24,** no. 1, 257–277.

Doser, D. I., and W. A. Brown (2001). A study of historic earthquakes of the Prince William Sound, Alaska, region, *Bull. Seismol. Soc. Am.* **91,** no. 4, 842–857.

Eberhart-Phillips, D., D. H. Christensen, T. M. Brocher, R. Hansen, N. A. Ruppert, P. J. Haeussler, and G. A. Abers (2006). Imaging the transition from Aleutian subduction to Yakutat collision in central Alaska, with local earthquakes and active source data, *J. Geophys. Res.* **111,** doi: 10.1029/2005JB004240.

Feng, L., and M. H. Ritzwoller (2017). The effect of sedimentary basins on surface waves that pass through them, *Geophys. J. Int.* **211,** 572–592, doi: 10.1093/gji/ggx313.

Field, E., and K. Jacob (1993). The theoretical response of sedimentary layers to ambient seismic noise, *Geophys. Res. Lett.* **20,** no. 24, 2925–2928.

Fisher, M. A., and L. B. Magoon (1978). Geologic framework of lower Cook Inlet, *Am. Assoc. Petrol. Geol. Bull.* **62,** no. 3, 373–402.

Fletcher, J. B., and K.-L. Wen (2005). Strong ground motion in the Taipei basin from the 1999 Chi-Chi, Taiwan, earthquake, *Bull. Seismol. Soc. Am.* **95,** no. 4, 1428–1446, doi: 10.1785/0120040022.

Frankel, A. (1993). Three-dimensional simulations of ground motions in the San Bernadino Valley, California, for hypothetical earthquakes on the San Andreas fault, *Bull. Seismol. Soc. Am.* **83,** no. 4, 1020–1041.

Frankel, A., W. Stephenson, and D. Carver (2009). Sedimentary basin effects in Seattle, Washington: Ground-motion observations and 3D simulations, *Bull. Seismol. Soc. Am.* **99,** no. 3, 1579–1611, doi: 10.1785/0120080203.

Grapenthin, R., M. West, C. Tape, M. Gardine, and J. Freymueller (2018). Single-frequency instantaneous GNSS velocities resolve dynamic ground motion of the 2016 M_w 7.1 Iniskin, Alaska, earthquake, *Seismol. Res. Lett.* **89,** no. 3, 1040–1048, doi: 10.1785/0220170235.

Graves, R. W., A. Pitarka, and P. G. Somerville (1998). Ground-motion amplification in Santa Monica area: Effects of shallow basin-edge structure, *Bull. Seismol. Soc. Am.* **88,** no. 5, 1224–1242.

Gregersen, L. S., and D. P. Shellenbaum (2016). Top Mesozoic unconformity subcrop map, Cook Inlet basin, Alaska, *Alaska Div. Geol. Geophys. Surv. Report of Investigation 2016-4*, 1 sheet, Scale 1:500,000, available at http://www.dggs.alaska.gov/pubs/id/29658 (last accessed October 2016).

Gutenberg, B. (1957). Effects of ground on earthquake motion, *Bull. Seismol. Soc. Am.* **47,** no. 3, 221–250.

Haeussler, P. J., R. L. Bruhn, and T. L. Pratt (2000). Potential seismic hazards and tectonics of the upper Cook Inlet basin, Alaska, based on analysis of Pliocene and younger deformation, *Geol. Soc. Am. Bull.* **112,** no. 9, 1414–1429.

Hayes, G. P., G. L. Moore, D. E. Portner, M. Hearne, H. Flamme, M. Furtney, and G. M. Smoczyk (2018). Slab2, a comprehensive subduction zone geometry model, *Science* **362,** doi: 10.1126/science.aat4723.

Hisada, Y., and S. Yamamoto (1996). One-, two-, and three-dimensional site effects in sediment-filled basins, *Proceedings on the Eleventh World Conference Earthquake Engineering*, Acapulco, Mexico, 23–28 June 1996, Paper Number 2040.

Incorporated Research Institutions for Seismology (IRIS) (2003). USArray Transportable Array. International Federation of Digital Seismograph Networks, Other/Seismic Network, doi: 10.7914/SN/TA.

Joyner, W. (2000). Strong motion from surface waves in deep sedimentary basins, *Bull. Seismol. Soc. Am.* **90,** no. 6B, S95–S112.

Kawase, H. (1996). The cause of the damage belt in Kobe: "The basin-edge effect," constructive interference of the direct S-wave with the basin-induced diffracted/Rayleigh waves, *Seismol. Res. Lett.* **67,** no. 5, 25–34.

Koehler, R. D., R.-E. Farrell, P. A. C. Burns, and R. A. Combellick (2012). Quaternary faults and folds in Alaska: A digital database, *Alaska Div. Geol. Geophys. Surv. Miscellaneous Publication 141*, 1 sheet, Scale 1:3,700,000, 31 pp., doi: 10.14509/23944.

Krischer, L., T. Mengies, R. Barsch, M. Beyreuther, T. Lecocq, C. Caudron, and J. Wassermann (2015). ObsPy: A bridge for seismology into the scientific Python ecosystem, *Comput. Sci. Discov.* **8,** no. 1, doi: 10.1088/1749-4699/8/1/014003.

Lawson, A. C. (1908). *The California Earthquake of April 18, 1906: Report of the State Earthquake Investigation Commission in Two Volumes and Atlas*, Vol. 1, Carnegie Institution, Washington, D.C.

Li, J., G. A. Abers, Y. Kim, and D. Christensen (2013). Alaska megathrust 1: Seismicity 43 years after the great 1964 Alaska megathrust earthquake, *J. Geophys. Res.* **118,** 4861–4871, doi: 10.1002/jgrb.50358.

Liu, C., T. Lay, Z. Xie, and X. Xiong (2019). Intraslab deformation in the 30 November 2018 Anchorage, Alaska, M_w 7.1 earthquake, *Geophys. Res. Lett.* **46,** 2449–2457, doi: 10.1029/2019GL082041.

Lomnitz, C. (1988). The 1985 Mexico earthquake, in M. I. El-Sabh and T. S. Murty (Editors), *Natural and Man-Made Hazards: Proceedings of the International Symposium*, Rimouski, Quebec, Canada, 3–9 August 1986, 63–79.

McNamara, D. E., and R. P. Buland (2004). Ambient noise levels in the continental United States, *Bull. Seismol. Soc. Am.* **94,** no. 4, 1517–1527, doi: 10.1785/012003001.

Moschetti, M. P., S. Hartzell, L. Ramírez-Guzmán, A. D. Frankel, S. J. Angster, and W. J. Stephenson (2017). 3D ground-motion simulations of M_w 7 earthquakes on the Salt Lake City segment of the Wasatch fault zone: Variability of long-period ($T \geq 1$ s) ground motions and sensitivity to kinematic rupture parameters, *Bull. Seismol. Soc. Am.* **107,** no. 4, 1704–1723, doi: 10.1785/0120160307.

Moschetti, M. P., E. M. Thompson, J. Rekoske, M. G. Hearne, P. M. Powers, D. McNamara, and C. Tape (2020). Ground-motion amplification in Cook Inlet region, Alaska from the 2018 M_w 7.1 Anchorage earthquake and intermediate-depth earthquakes, *Seismol. Res. Lett.* doi: 10.1785/0220190179.

National Oceanic and Atmospheric Administration (NOAA) (1967). National Tsunami Warning Center Alaska Seismic Network. International Federation of Digital Seismograph Networks, Other/Seismic Network, doi: 10.7914/SN/AT.

Olsen, K. B. (2000). Site amplification in the Los Angeles basin from three-dimensional modelling of ground motion, *Bull. Seismol. Soc. Am.* **60,** no. 6B, S77–S94, doi: 10.1785/0120000506.

Peterson, J. (1993). Observations and modeling of seismic background noise, *U.S. Geol. Surv. Open-File Rept. 93-322*, 94 pp.

Pratt, T. L., T. M. Brocher, C. S. Weaver, K. C. Creager, C. M. Snelson, R. S. Crosson, K. C. Miller, and A. M. Trehu (2003). Amplification of seismic waves by the Seattle basin, Washington state, *Bull. Seismol. Soc. Am.* **93,** no. 2, 533–545.

Rial, J. A., N. G. Saltzman, and H. Ling (1992). Earthquake-induced resonance in sedimentary basins, *Am. Sci.* **80,** 566–578.

Saltus, R. W., R. G. Stanley, P. J. Haeussler, J. V. Jones III, C. J. Potter, and K. A. Lewis (2016). Late Oligocene to present contractional structure in and around the Susitna basin, Alaska—Geophysical evidence and geological implications, *Geosphere* **12,** no. 5, 1–13, doi: 10.1130/GES01279.1.

Sánchez-Sesma, F., and F. Luzón (1995). Seismic response of three-dimensional alluvial valleys for incident *P*, *S*, and Rayleigh waves, *Bull. Seismol. Soc. Am.* **85,** no. 1, 269–284.

Shellenbaum, D. P., L. S. Gregersen, and P. R. Delaney (2010). Top Mesozoic unconformity depth map of the Cook Inlet Basin, Alaska, *Alaska Div. Geol. Geophys. Surv. Report of Investigation 2010-2*, 1 sheet, Scale 1:500,000, available at http://www.dggs.alaska.gov/pubs/id/21961 (last accessed October 2016).

Silwal, V., and C. Tape (2016). Seismic moment tensors and estimated uncertainties in southern Alaska, *J. Geophys. Res.* **121,** 2772–2797, doi: 10.1002/2015JB012588.

Silwal, V., C. Tape, and A. Lomax (2018). Crustal earthquakes in the Cook Inlet and Susitna region of southern Alaska, *Tectonophysics* **745,** 245–263, doi: 10.1016/j.tecto.2018.08.013.

Smith, K. (2019). Supplement to "Seismic response of Cook Inlet sedimentary basin, southern Alaska", *ScholarWorks@UA*, descriptor file, figures of seismic noise spectra, ground motion metrics, and spectral ratios, available at http://hdl.handle.net/11122/10568 (last accessed July 2019).

Sorrells, G. G., J. A. McDonald, Z. A. Der, and E. Herrin (1971). Earth motion caused by local atmospheric pressure changes, *Geophys. J. Roy. Astron. Soc.* **26,** 83–98.

Stanley, R. G., P. J. Haeussler, J. A. Benowitz, D. K. Goodman, R. L. Ravn, D. P. Shellenbaum, R. W. Saltus, K. A. Lewis, and C. J. Potter (2013). New stratigraphic revelations in the subsurface Susitna basin, south-central Alaska, from geochronology and biostratigraphy [poster], *GSA Cordilleran Section Meeting*, Fresno, California, 22 May 2013, Alaska Division of Geological & Geophysical Surveys, 1 sheet, doi: 10.14509/26887.

Stein, S., and M. Wysession (2003). *An Introduction to Seismology, Earthquakes, and Earth Structure*, Blackwell, Malden, Massachusetts.

Tape, C., D. Christensen, and M. M. Moore-Driskell (2015). Southern Alaska Lithosphere and Mantle Observation Network. International Federation of Digital Seismograph Networks, Other/Seismic Network, doi: 10.7914/SN/ZE_2015.

Tape, C., D. Christensen, M. M. Moore-Driskell, J. Sweet, and K. Smith (2017). Southern Alaska Lithosphere and Mantle Observation Network (SALMON): A seismic experiment covering the active arc by road, boat, plane, and helicopter, *Seismol. Res. Lett.* **88,** no. 4, 1185–1202, doi: 10.1785/0220160229.

Tape, C., D. C. Heath, M. G. Baker, S. Dalton, K. Aderhold, and M. E. West (2019). Bear encounters with seismic stations in Alaska and northwestern Canada, *Seismol. Res. Lett.* **90,** no. 5, 1950–1970.

Tong, P., D. Komatitsch, T.-L. Tseng, S.-H. Hung, C.-W. Chen, P. Basini, and Q. Liu (2014). A 3-D spectral-element and frequency-wave number hybrid method for high-resolution seismic array imaging, *Geophys. Res. Lett.* **41,** 7025–7034, doi: 10.1002/2014GL061644.

Tsai, V. C., D. C. Bowden, and H. Kanamori (2017). Explaining extreme ground motion in Osaka basin during the 2011 Tohoku earthquake, *Geophys. Res. Lett.* **44,** 7239–7244, doi: 10.1002/2017GL074120.

Wald, D. J., and R. W. Graves (1998). The seismic response of the Los Angeles basin, California, *Bull. Seismol. Soc. Am.* **88,** no. 2, 337–356.

Wang, Y., and C. Tape (2014). Seismic velocity structure and anisotropy of the Alaska subduction zone derived from surface wave tomography, *J. Geophys. Res.* **119,** 8845–8865, doi: 10.1002/2014JB011438.

Ward, K. M., and F.-C. Lin (2018). Lithospheric structure across the Alaskan cordillera from the joint inversion of surface waves and receiver functions, *J. Geophys. Res.* **123,** 8780–8797, doi: 10.1029/2018JB015967.

West, M. E., A. Bender, M. Gardine, L. Gardine, K. Gately, P. Haeussler, W. Hassan, F. Meyer, C. Richards, C. Tape, *et al.* (2019). The 30 November 2018 M_w 7.1 Anchorage earthquake, *Seismol. Res. Lett.* doi: 10.1785/0220190176.

Wirth, E. A., J. E. Vidale, A. D. Frankel, T. L. Pratt, N. A. Marafi, M. Thompson, and W. J. Stephenson (2019). Source-dependent amplification of earthquake ground motions in deep sedimentary basins, *Geophys. Res. Lett.* **46,** 6443–6450, doi: 10.1029/2019GL082474.

Yoshimoto, K., and S. Takemura (2014). A study on the predominant period of long-period ground motions in the Kanto Basin, Japan, *Earth Planets Space* **66,** doi: 10.1186/1880-5981-66-100.

Zweck, C., J. T. Freymueller, and S. C. Cohen (2002). Three-dimensional elastic dislocation modeling of the postseismic response to the 1964 Alaska earthquake, *J. Geophys. Res.* **107,** no. B4, doi: 10.1029/2001JB000409.

Manuscript received 31 July 2019
Published online 30 October 2019